Chapter 4

Quantum dynamics and control

This chapter focuses on the analysis and control of bond selective dissociation in the two model systems, FHF^- and OHF^-, using ultrashort few-cycle IR and UV laser pulses. Before the results of the wave packet propagations are presented, the general approach, including the design of half-cycle and few-cycle laser pulses, will be discussed in detail in Section 4.1. The review of the electric field is particularly helpful in understanding the nature of the field-matter interaction in the subsequent discussion of wave packet dynamics results.

Next, in Section 4.3, bond-selective dissociation will be investigated for *pre-oriented* FHF^- molecules. In other words, the linear triatomic molecule is assumed to be oriented in the laboratory frame prior to the wave packet simulations. These results will be followed by a comparison of the molecular dynamics of FHF^- with those of the heavier isotopomer, FDF^-. This section will conclude with a discussion of the effect of random molecular orientation on the selectivity and efficiency of the proposed IR + UV laser pulse scheme.

Finally, the bond-selective dissociation of OHF^- will be discussed in Section 4.4. First, the molecular orientation of OHF^- in the space-fixed laboratory frame will be treated *explicitly*. A half-cycle pulse (HCP) will be designed to give the molecule a "kick" of angular momentum in the direction of the laser field polarization. The resulting rotational wave packets will be propagated to obtain quantitative information about the extent of molecular orientation of the OHF^- molecules. Next, ultrashort few-cycle IR and UV laser pulses will be optimized to achieve bond-selective dissociation in the OHF^- molecules that have been oriented in the space-fixed (laboratory) frame. Chapter 4 will conclude with a discussion of possible sources of error (Section 4.5).

4.1 Approach

The approach to control molecular orientation and subsequent bond-selective dissociation, as first described in Chapter 1, is as follows: a linearly (Z) polarized, half-cycle far-IR (THz) pulse of width $\sigma \approx 200 - 300$ fs is applied to a randomly oriented molecule. The laser field exerts a force on the molecular axis, such that the angle between the molecular axis and the polarization direction, θ, is restricted. The rotational motion (librations) of the molecule becomes confined in angular space and the molecule becomes oriented in the electric field. Due to the quantum dynamical nature of the wave packet, dephasing and rephasing of rotational eigenstates occurs, on a time scale governed by the rotational period of the molecules. These rotational revivals are observed over hundreds of picoseconds, during which a high degree of orientation is periodically realized. When orientation is maximum, lasting several picoseconds, a second, short ($t_p < 100$ fs) few-cycle IR laser pulse is applied to drive the asymmetric stretching vibration of the anion; this mode is equivalent to the oscillation of the hydrogen between the two end atoms. With each cycle of the pulse, the hydrogen is pushed farther away from its equilibrium position. When the displacement of the hydrogen is at a maximum, an ultrashort ($t_p \approx 5$ fs) UV pulse is applied, whose frequency is sufficient to detach an electron from the anion. The neutral species is now located primarily in a dissociation channel that corresponds to the breaking of the already extended bond. The molecule proceeds to dissociate, with dissociation products spatially localized according to the orientation of the anion in the space-fixed frame. In this manner, an optimized IR + IR + UV laser pulse sequence can achieve bond-selective dissociation of randomly oriented molecules; this mechanism is shown schematically in Figure 4.1. In the next section, the design of such pulse sequences will be discussed in detail, followed by the presentation of the results obtained for the bond-selective dissociation of FHF^- and OHF^-.

4.2 Time-dependent Schrödinger equation for a coupled two-level system

The laser-driven dynamics is simulated with nuclear wave packets that are obtained as solutions of the time-dependent Schrödinger equation, introduced for a coupled two-level system in Eq. (2.115). Now, we specify that the two-level system consists of an anionic state, indicated with the subscript a, and a neutral state, indicated with the subscript n:

$$i\hbar\frac{\partial}{\partial t}\begin{pmatrix} |\Psi_a(t)\rangle \\ |\Psi_n(t)\rangle \end{pmatrix} = \begin{pmatrix} \hat{\mathbf{H}}_a & \hat{\mathbf{H}}_{an} \\ \hat{\mathbf{H}}_{na} & \hat{\mathbf{H}}_n \end{pmatrix}\begin{pmatrix} |\Psi_a(t)\rangle \\ |\Psi_n(t)\rangle \end{pmatrix}, \tag{4.1}$$

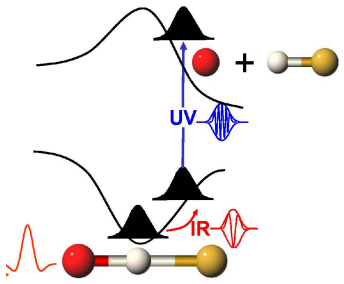

Figure 4.1: An optimized IR + IR + UV laser pulse sequence achieves bond-selective dissociation. A half-cycle IR pulse orients the molecule in the space-fixed (laboratory) frame. A second, few-cycle IR pulse drives the asymmetric stretching vibration of the triatomic molecule, equivalent to pushing the center hydrogen away from its equilibrium position. When displacement of the hydrogen is at a maximum, an ultrashort ($t_p \approx 5$ fs) UV pulse is applied, whose frequency is sufficient to detach an electron from the anion. The neutral species is now located primarily in a dissociation channel that corresponds to the breaking of the already extended bond. Due to the orientation of the anionic species—and therefore of its neutral counterpart—the dissociation products will have a well-defined spatial separation.

The wave functions $|\Psi_a(t)\rangle$ and $|\Psi_n(t)\rangle$ are the 1D or 2D wave functions of the anion and neutral molecule, respectively. The Hamiltonian is given as

$$\begin{pmatrix} \hat{\mathbf{H}}_a & \hat{\mathbf{H}}_{an} \\ \hat{\mathbf{H}}_{na} & \hat{\mathbf{H}}_n \end{pmatrix} = \begin{pmatrix} \hat{\mathbf{T}} + \hat{\mathbf{V}}_a - \vec{\boldsymbol{\mu}}_a \cdot \vec{E}(t) & -\vec{\boldsymbol{\mu}}_{an} \cdot \vec{E}(t) \\ -\vec{\boldsymbol{\mu}}_{na} \cdot \vec{E}(t) & \hat{\mathbf{T}} + \hat{\mathbf{V}}_n - \vec{\boldsymbol{\mu}}_n \cdot \vec{E}(t) \end{pmatrix} \tag{4.2}$$

The diagonal terms of the Hamiltonian, $\hat{\mathbf{H}}_{ii}$, consist of the kinetic ($\hat{\mathbf{T}}$) and potential ($\hat{\mathbf{V}}$) energies of the system, and the time-dependent potential energy arising from the interaction of the permanent dipole moments, $\vec{\boldsymbol{\mu}}_a$ and $\vec{\boldsymbol{\mu}}_n$, with the external electric field, $\vec{E}(t)$. The permanent dipole moment of the anion species is calculated with *ab initio* methods, and as the PES, it depends parametrically on the nuclear coordinates, $\vec{\boldsymbol{\mu}}_a \equiv \vec{\boldsymbol{\mu}}_a\{\vec{R}_A\}$. The permanent dipole moment of the neutral species $\vec{\boldsymbol{\mu}}_n$ has been set equal to 0 since vibrational transitions in the neutral PES are not considered. The off-diagonal elements of the Hamiltonian, $\hat{\mathbf{H}}_{ij}$, are transition dipole terms. Within the Condon approximation, the transition dipole moment can be considered constant with respect to a reference nuclear configuration, and for simplicity, it is set equal to 1 [121]:

$$\vec{\boldsymbol{\mu}}_{na} = \vec{\boldsymbol{\mu}}_{an} = 1. \tag{4.3}$$

Within this model consisting of two coupled states, population can travel from the anionic PES V_a to the neutral PES V_n and vice versa, according to the perturbation potentials $-\vec{\boldsymbol{\mu}}_{an} \cdot \vec{E}(t)$ and $-\vec{\boldsymbol{\mu}}_{na} \cdot \vec{E}(t)$, respectively. However, since we are modelling the photodetachment of an electron via a UV laser pulse, the back-transfer of population from the neutral to anionic state would correspond to the re-attachment of an electron to the molecule, a process that is physically impossible under normal experimental conditions. Therefore, to ensure that this artificial back-transfer is kept to a minimum,

the laser intensity is chosen low enough ($< 10^{13}$ W/cm^2) such that no more than $\sim 10\%$ of the initial population in the anionic state is excited to the neutral PES. Under these conditions, a back-transfer of population from V_n to V_a is limited to $\sim 1\%$. Therefore, although this back-transfer is an artifact of the model and physically unrealistic, it can be considered negligibly small.

In the upcoming simulations, the time-dependent electric field, $\vec{E}(t)$, is a laser field consisting of either a single half-cycle or few cycles. As mentioned earlier (see Section 2.3.2), we assume that the analytical expressions used to describe these pulses are a good approximation to experimentally reproducible few-cycle pulses. The design and applications of such fields will be discussed next, beginning with HCPs.

4.2.1 Half-cycle IR orientation pulse

A pulse consisting of a single half-cycle (HCP) was introduced in Section 2.5.3 in the context of orienting an ensemble of rigid molecules. In this thesis, the linearly polarized HCPs used (Eqs. (2.224) and (2.225)) are Gaussian in shape and consist of predominantly one field polarization,

$$E(t) = \vec{\varepsilon} E_0 \cos(\omega t + \varphi) e^{-(t-t_0)^2/\sigma^2}, \tag{4.4}$$

where $\vec{\varepsilon}$ is a unit vector along the polarization direction, taken by convention to be along the Z axis in the laboratory frame, E_0 is the field strength, ω is the frequency, φ is the phase, t_0 is the time at which the pulse is centered, and σ is the pulse width. The field strength E_0 is chosen such that high intensities are avoided, *i.e.* $I_{\max} < 10^{13}$ W/cm^2 (see Eq. (2.139)). The pulse width, σ (*cf.* Eq. (2.136)), is chosen to be shorter than the rotational period, $\sigma < \tau_{\text{rot}} (\equiv \pi\hbar/B)$, which is calculated to be 49.6 ps for OHF^-. The central carrier frequency, ω, is tuned to be off-resonant with vibrational and electronic transitions. This condition implies far-IR frequencies, $\omega \leq 200$ cm^{-1}. An exemplary HCP is shown in Figure 4.2.

4.2.2 Few-cycle IR pulses

Few-cycle pulses were introduced in Section 2.3.2, and we will now discuss in detail the design of the pulses used in our quantum dynamics simulations. This discussion is intended to be didactic and will therefore provide a step-by-step guide to building a smooth $\sin^2$-pulse, as used in the upcoming simulations.

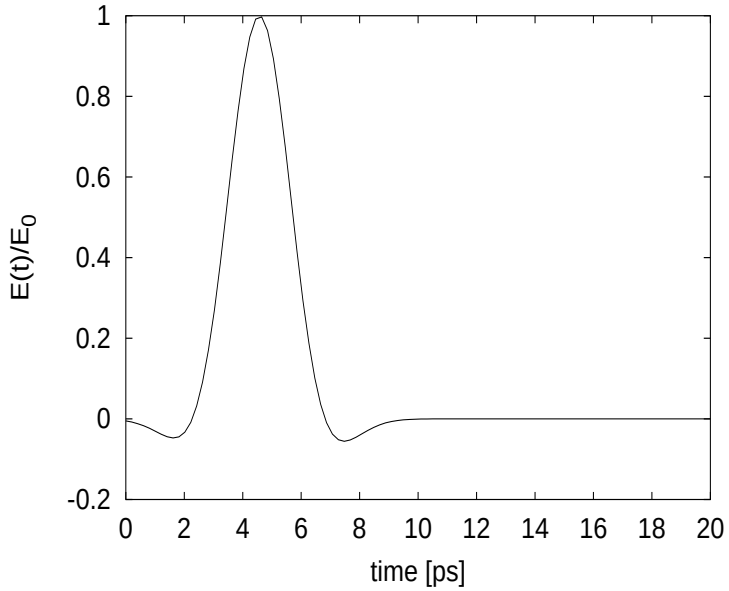

Figure 4.2: A Gaussian-shaped HCP, given in Eq. (4.4), with pulse parameters $\omega = 23.4$ cm^{-1}, $\varphi = 0$, $t_0 = 4.6$ ps, and $\sigma = 2$ ps (FWHM).

The excitation of the asymmetric stretching vibration in XHY^- type anions is equivalent to driving the oscillation of the hydrogen atom between the heavy end atoms. An IR laser pulse that excites this mode should therefore have the following characteristic: one half-cycle of the electric field oscillation, $\frac{1}{2}(2\pi/\omega_{\rm IR})$, should match half the period of the asymmetric stretching vibration, $\tau_{as}/2$, or simplified,

$$\frac{\pi}{\omega_{\rm IR}} = \frac{\tau_{as}}{2}. \tag{4.5}$$

In other words, the frequency of the IR laser pulse, $\omega_{\rm IR}$, should be tuned to match the natural asymmetric stretching vibration of the system. For a single half-cycle laser pulse, $t_p = \frac{1}{2}\tau_{\rm IR} = \frac{\pi}{\omega_{\rm IR}}$, where $\tau_{\rm IR}$ is the period of the IR light. In other words, the IR pulse frequency is just given by

$$\omega_{\rm IR} = \frac{\pi}{t_p}, \tag{4.6}$$

so that $\omega_{\rm IR}$ can now be replaced in the laser field expression. For a pulse containing a single half-cycle, the laser field can be written

$$\vec{E}(t) = \begin{cases} \vec{\varepsilon} E_0 \sin\left(\frac{\pi}{t_p}(t - t_0)\right) & t_0 \leq t \leq (t_0 + t_p) \\ 0 & \text{otherwise,} \end{cases} \tag{4.7}$$

where t_0 is the time at which the pulse starts. This half-cycle pulse, shown in Figure 4.3, is similar in shape to the Gaussian pulse shown in Figure 4.2, but it lacks the smooth turn-on and turn-off behavior of the Gaussian pulse. For a "short" pulse duration, $t_p \leq 100$ fs ($\omega_{\rm IR} \simeq 1000 - 2000$ cm^{-1}), the field described in Eq. (4.7) exerts a brief force on the charge distribution (permanent dipole moment) of the molecule and

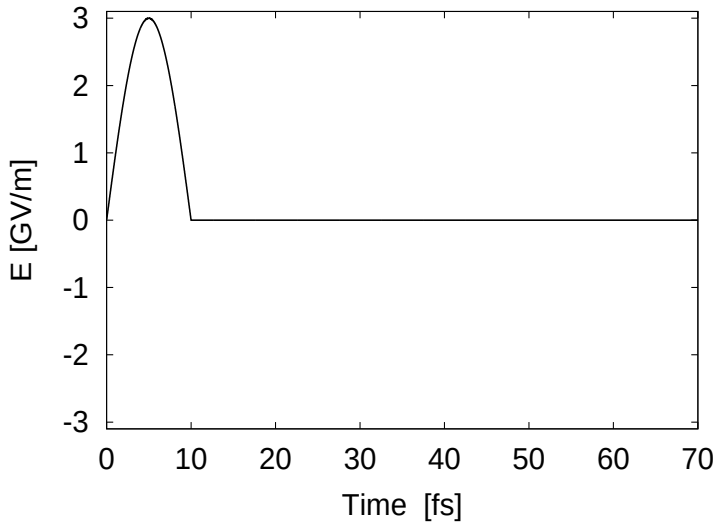

Figure 4.3: A half-cycle sin-pulse, given in Eq. (4.7), with pulse parameters $E_0 = 3.0$ GV/m, $t_0 = 0$ fs, and $t_p = 10$ fs.

induces a time-dependent change in the potential energy of the system. If this energy is resonant with natural vibrational energies, the corresponding vibrational transition will take place. In this case, the spectral width of the 10 fs laser pulse $\Delta\omega = 265$ cm^{-1} (see Eq. (2.141)), and for mid-IR frequencies (~ 1500 cm^{-1}), this spectral bandwidth is approximately $\Delta\omega/\omega \approx 0.18$. Therefore, a superposition of asymmetric stretching vibrational eigenstates—or a wave packet—is excited, and the effect is a brief "kick" applied to the hydrogen such that it begins oscillating. If one HCP is expected to push the center hydrogen away from its equilibrium position, several half-cycle pulses applied to the system would cause even larger bond extensions than a single half-cycle pulse, similar to a swing being pushed each time it reaches its minimum. A series of three such HCPs, each given by Eq. (4.7), is shown in Figure 4.4, in which the sign of the electric field is reversed with each HCP. One could imagine applying several HCPs, each of which would push the hydrogen farther and farther away from its equilibrium position. However, the vibrational wave packet that is created simultaneously undergoes dispersion due to anharmonicity of the PES, so this competing effect must also be considered over longer times. Since a compact wave packet is typically desired for maximum population transfer, wave packet propagation times and pulse durations should be kept short relative to dispersion time scales.

Three HCPs can be replaced by a single $\sin^2$-shaped pulse with an average IR carrier frequency, ω_{IR}, that smoothly turns on and off, as introduced in Eq. (2.138) and given by

$$\vec{E}(t) = \begin{cases} \vec{\varepsilon} E_0 \, \sin(\omega_{\mathrm{IR}} t + \varphi) \, \sin^2\left(\frac{\pi(t-t_0)}{t_p}\right) & t_0 \leq t \leq (t_0 + t_p) \\ 0 & \text{otherwise,} \end{cases} \tag{4.8}$$

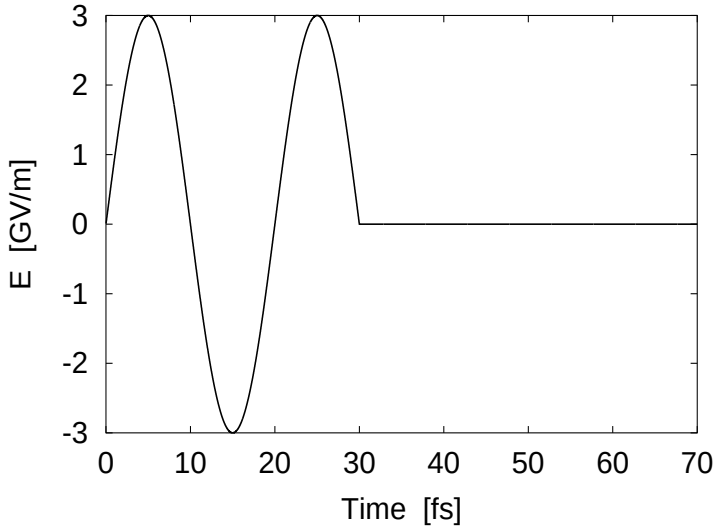

Figure 4.4: An IR laser pulse consisting of three 10 fs half-cycles. The laser field is given in Eq. (4.7). The laser parameters for each HCP are:
$E_{0,1} = +3.0$ GV/m, $t_{0,1} = 0$ fs, and $t_{p1} = 10$ fs;
$E_{0,2} = -3.0$ GV/m, $t_{0,2} = 10$ fs, and $t_{p2} = 10$ fs;
$E_{0,3} = +3.0$ GV/m, $t_{0,3} = 20$ fs, and $t_{p3} = 10$ fs.

where φ is the pulse phase, t_0 is the time at which the pulse is applied, and t_p is the pulse duration governing the number of field cycles that are contained within the pulse envelope. A smooth pulse that mimics the pulse containing three half-cycle pulses is shown in Figure 4.5. This pulse consists of five half-cycles, but the similarity of this IR pulse with the previous series of half-cycle pulses is apparent: both contain three dominant peaks with similar field strengths and duration (*cf.* Figure 4.4). The pulse parameters are $\omega_{\mathrm{IR}} = 2\pi/\tau_{\mathrm{IR}} = 1516$ cm^{-1}, $\varphi = 0$, $t_0 = 0$, and $t_p \approx 5\,\tau_{\mathrm{IR}}/2 = 55$ fs. Since only the peak of the shaped pulse in Figure 4.5 reaches the full amplitude of the half-cycle pulses, the magnitude of the field strength, $|E_0|$, must be increased, *e.g.* from 3.0 GV/m to 4.0 GV/m (*cf.* Figures 4.4 and 4.5), to deliver the same power spectrum as the series of three half-cycle pulses.[1]

An important quality of ultrashort laser pulses is their spectral width. In other words, the uncertainty principle, discussed in Section 2.3.3, demands that temporally narrow pulses be energetically broad; the shorter the duration of the pulse, the broader the spread of frequencies contained within the pulse envelope. For a $\sim$ 50 fs pulse centered in the IR frequency domain, *i.e.* $\omega = 1516$ cm^{-1} (corresponding to a wavelength $\lambda \approx 1064$ nm), the spectral bandwidth is $\Delta\omega = 53$ cm^{-1}. This spread is relatively narrow, $\Delta\omega/\omega \sim 0.03$ cm^{-1}. Nonetheless, the range of frequencies 1516 ± 53 cm^{-1} present in the IR laser pulse is essential for exciting several vibrational modes simultaneously—or a

[1] The power spectrum describes energy per unit time, and, unlike the frequency spectrum, it contains no spatial or phase information.

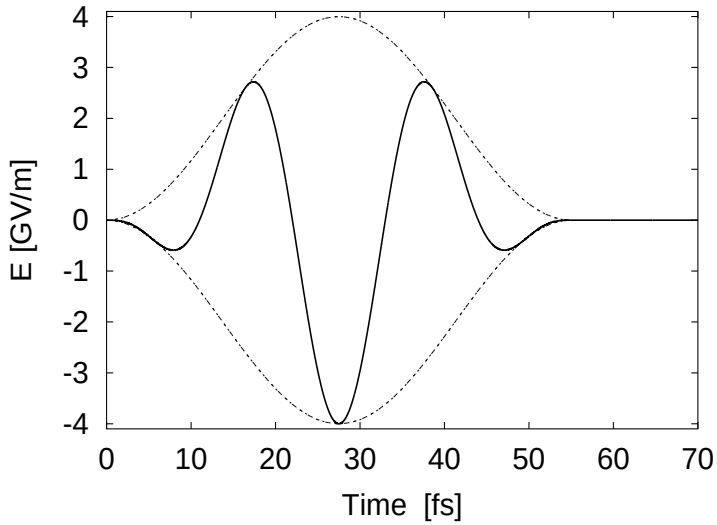

Figure 4.5: A smooth $\sin^2$-shaped IR laser pulse, as given in Eq. (4.8), consists of approximately five 10 fs half-cycles. Pulse parameters are $E_0 = -4$ GV/m, $\omega = 1516$ cm^{-1}, $\varphi = 0$, $t_0 = 0$ fs, and $t_p = 55$ fs.

superposition of eigenfunctions—and therefore creating a wave packet. Indeed, a cw laser would only be capable of initiating a single vibrational transition, whereas ultrashort laser pulses can simultaneously excite several vibrational eigenstates due to their spectral width.

4.2.3 UV pulses

When the appropriate bond has been maximally extended by the few-cycle IR pulse, an ultrashort, $t_p < 5$ fs, UV pulse can be applied to excite vertically the displaced wave packet to the neutral surface. This pulse is also a smooth $\sin^2$-pulse, given in Eq. (4.8). The frequency of the UV light should be chosen such that it matches the vertical energy spacing between the anionic and neutral PESs, $\omega_{\mathrm{UV}} = (\mathrm{V}_n - \mathrm{V}_a)/\hbar$, as depicted in Figure 4.1. As discussed in Section 2.3.3, a 5 fs UV pulse centered at 43 500 cm^{-1} has a spectral bandwidth of $\sim$530 cm^{-1}, or $\sim$0.07 eV. This bandwidth could, therefore, cause the wave packet to be excited to anionic electronic excited states if they are located at $43\,500 \pm 530$ cm^{-1}, *i.e.* in the vicinity of the ground PES of the neutral species, V_n. In this thesis, however, only the ground PESs of the anion and neutral species were included in the simulations.

In the next section, the optimized parameters for each laser pulse will be discussed and the resulting wave packet dynamics will be presented. In general, time-dependent wave packets for the anionic and neutral systems will be denoted $\Psi_a(t)$ and $\Psi_n(t)$, respectively, whereas vibrational eigenstates will be denoted v, either v_{as} in the 1D case or $v_{s\,as}$ in the

2D case.

4.3 Results for FHF^-/FHF

This section will focus on the results obtained for the first anion/neutral model system that was studied, FHF^-/FHF. Few-cycle IR laser pulse parameters for the bond-selective dissociation of FHF^- were optimized first within a 1D model and then extended to a 2D model. Wave packets obtained as solutions to the time-dependent Schrödinger equation were calculated with the split-operator method [138, 139], using a time step $\Delta t = 0.01$ fs. No absorbing boundary function was implemented in the wave packet simulations for FHF^-/FHF.

In the 1D model, the coordinate that was considered was the asymmetric stretching coordinate, defined $q_{as} = \frac{1}{2}(R_1 - R_2)$, that is, the distance between the hydrogen and the center of mass of the two fluorine atoms. For $q_{as} = 0$, the bond distances are equal and the molecule is in its equilibrium geometry. The spatial discretization of the 1D anionic and neutral potential energy curves, and anionic permanent dipole curve, consisted of $\mathcal{N} = 128$ grid points for each curve. The grid points were obtained from a cubic spline of 23 QCISD *ab initio* points. For the calculation of the *ab initio* points, the coordinate q_{as} was varied from -0.6 Å to $+0.6$ Å in steps of 0.054 Å.

The 2D PESs were constructed in the bond distances $R_1(\equiv F_a - H)$ and $R_2(\equiv F_b - H)$ (see Section 3.2.1 for more details), and $\mathcal{N} = 64 \times 64 = 4096$ bi-cubically splined points were used for the PES for the wave packet simulations. The coordinate $q_{as} = \frac{1}{2}(R_1 - R_2)$ is retained to describe the displacement of the hydrogen between the end atoms. Branching ratios of the anion and neutral wave packets were obtained by summing the normalized population density over the two grid halves. In the 1D case, this summation of $|\Psi_{a,n}(q_{as}, t)|^2$ was performed over the grid halves $q_{as} > 0$ and $q_{as} < 0$, and in the 2D case $|\Psi_{a,n}(R_1, R_2, t)|^2$ was calculated over the grid halves $R_1 > R_2$ and $R_2 > R_1$ of the anionic and neutral surfaces. No absorbing boundary function was implemented in the wave packet simulations of FHF^-/FHF since the grid was sufficiently large for the duration of the propagations.

4.3.1 1D model

In the 1D model, QCISD/*d*-aug-cc-pVTZ potential energy curves for the collinear FHF^- and FHF systems (Figure 4.6(a)) and dipole curve (Figure 4.6(b)) for the anion were generated under C_{2v} symmetry, assuming the molecular axis lies along the space-fixed Z axis. The frequency of the asymmetric stretching vibration—the motion that is driven by

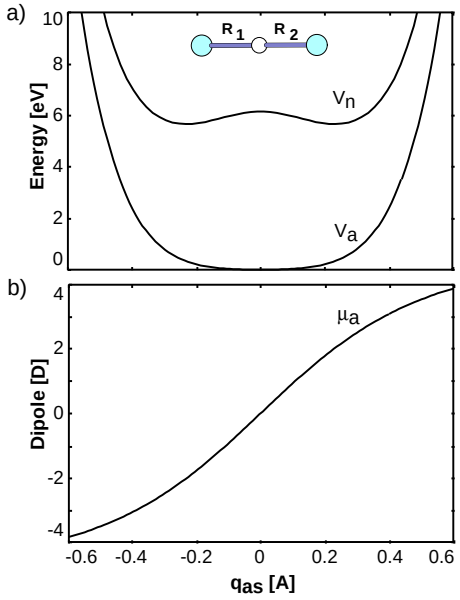

Figure 4.6: (a) QCISD/*d*-aug-cc-pVTZ potential energy (eV) curve for FHF^- (V_a) and FHF (V_n). (b) QCISD/*d*-aug-cc-pVTZ permanent dipole (Debye) curve for FHF^-. The coordinate q_{as} is defined $q_{as} = \frac{1}{2}(R_1 - R_2)$.

the IR laser pulse—for the anharmonic 1D model is $1815 (\equiv \upsilon_1 \leftarrow \upsilon_0)$ cm^{-1}. Starting from the ground state wave function of the anion, $\Psi_a(t=0) = \upsilon_0$, we apply a single IR HCP, given by Eq. (4.7). The field strength is $E_0 = 3.0$ GV/m ($I_{max} = 2.4$ TW/cm^2), the pulse begins at $t_0 = 0$ fs, and the pulse duration is $t_p = 10$ fs, which is approximately half the period of the asymmetric stretch of the 1D model, $0.5\tau_{as} = 9$ fs. This pulse and the wave packet dynamics resulting from its application are shown in the left panels of Figure 4.7. To measure the efficacy of the laser pulse in displacing υ_0, we calculate the modulus of the autocorrelation function, equal to the population of the vibrational ground state of the anion,

$$P_a(\upsilon_0) = |\langle \upsilon_0 | \Psi_a(t > 0) \rangle|^2 \tag{4.9}$$

as well as the branching ratios for which the wave packet is localized in the region $q_{as} > 0$ or $q_{as} < 0$ of V_a. While the field is on, population moves from υ_0 to other vibrational states, such that a superposition of several vibrational eigenstates is created. The autocorrelation function (see Figure 4.7(b)) reflects this migration as $P_a(\upsilon_0)$ drops to ~ 0.9; after the laser pulse has been turned off, $P_a(\upsilon_0)$ remains constant and only the phases of the wave packet components change. The wave packet begins oscillating, and at $t = 9.5$ fs, close to the end of the laser pulse, the H atom has been maximally shifted from its equilibrium position ($q_{as} = 0$ Å), such that the mean displacement reaches 0.075 Å, as shown in Figure 4.7(c) and (e). The branching ratio of the anionic wave packet, is almost 0.8 at this time, as shown in Figure 4.7(d). The symmetry of the system will continue to be broken almost periodically, although the coherence of the wave packet suffers over long times due to anharmonicity. Also, although larger displacements of the wave packet can

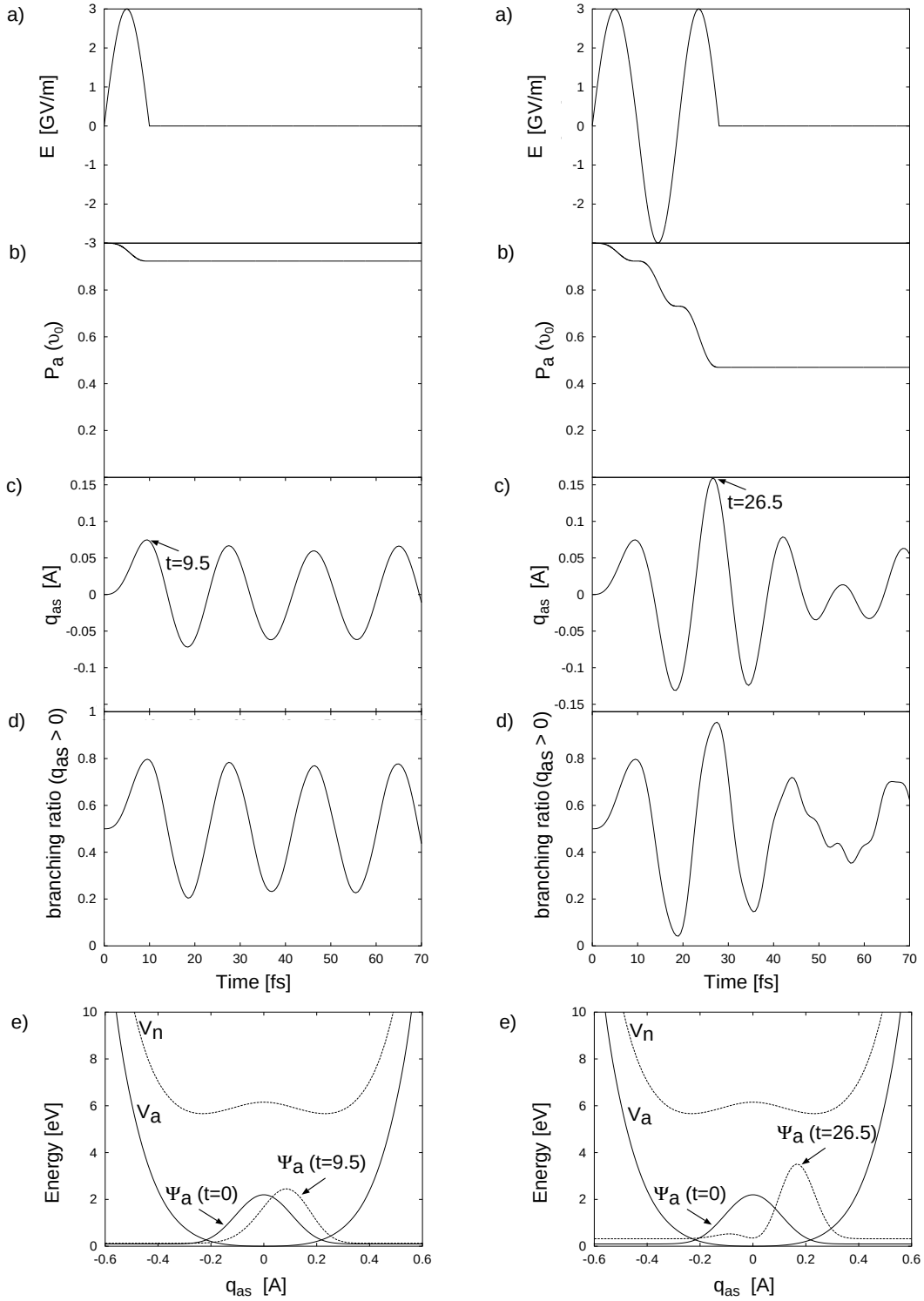

Figure 4.7: (a) Electric field vs. time. Left panel: A single HCP, electric field given in Eq. (4.7) with pulse parameters $E_0 = 3.0$ GV/m, $t_0 = 0$ fs, and $t_p = 10$ fs. Right panel: Three HCPs, electric field for each HCP given in Eq. (4.7) with following pulse parameters:
$E_{0,1} = 3.0$ GV/m, $t_{0,1} = 0$ fs, and $t_{p1} = 10$ fs;
$E_{0,2} = -3.0$ GV/m, $t_{0,2} = 10$ fs, and $t_{p2} = 9$ fs;
$E_{0,3} = 3.0$ GV/m, $t_{0,3} = 19$ fs, and $t_{p3} = 9$ fs.
(b) Population of the vibrational ground state of the anion, given by the modulus of the autocorrelation function, $P_a(\upsilon_0) = |\langle \upsilon_0 | \Psi_a(t > 0) \rangle|^2$. (c) Time evolution of the expectation value of the mean position of the H atom driven by the laser field shown in (a). (d) Branching ratio of species for which $q_{as} > 0$ vs. time. (e) Wave functions at time $t = 0$ fs (solid) and time corresponding to maximum displacement of the H atom (dotted), superimposed on the FHF^- potential curve.

be obtained by increasing the field strength, the competing effect of anharmonicity causes the wave packet to become less compact.

4.3.2 Three half-cycle pulses

Next, one half-cycle pulse is extended to a series of three HCPs with pulse durations $t_{p1} = 10$, $t_{p2} = 9$, and $t_{p3} = 9$ fs. The slight decrease in pulse durations is required since the oscillation is not harmonic. The magnitude of the field strength was maintained, but the sign is reversed for each pulse, *i.e.* $E_{0,1} = 3.0$ GV/m, $E_{0,2} = -3.0$ GV/m, and $E_{0,3} = 3.0$ GV/m. The effect of successive pulses can be compared to the classical situation of a driven oscillator; if the mass is pushed after passing through each turning point, the amplitude of the resulting oscillation will increase. The wave packet dynamics resulting from a series of three sin-pulses (Figure 4.7(a)) are shown in the right panel of Figure 4.7(b-d). This series of three half-cycle pulses achieves more pronounced excitation of the starting wave function υ_0, as indicated by the substantial decay of the ground state population, $P_a(\upsilon_0)$, shown in Figure 4.7(b). Each of the pulses leads to a greater displacement of the hydrogen from its equilibrium position until, at $t = 26.5$ fs, a maximum mean displacement of 0.16 Å is obtained, see Figures 4.7(c) and (e). If an ultrashort UV pulse were applied at 26.5 fs, the vertical transition would prepare the neutral FHF system in a configuration with similar geometry, namely with $q_{as} \approx 0.16$ Å. One can anticipate that the already stretched R_1 bond in the neutral system would proceed to break.

4.3.3 Extension to 2D model

In the next step of our investigation, the three sin-pulses applied to the 1D model are re-optimized to adapt to the 2D model; the corresponding wave packet dynamics are shown in the left panels of Figure 4.8. The lower 2D asymmetric stretching vibrational frequency, $1448 (\equiv \upsilon_{01} \leftarrow \upsilon_{00})$ cm^{-1}, compared to that of the 1D model, 1815 cm^{-1}, implies longer vibrational periods in the 2D model. The duration of the series of three half-cycle pulses driving the 2D wave function should, therefore, also be slightly longer than that of the 1D model. Accordingly, optimized laser parameters for the 2D system are $t_{p1} = 12$, $t_{p2} = 11$, and $t_{p3} = 11$ fs (slightly longer than the optimized values $t_{p1} = 11$, $t_{p2} = 10$, and $t_{p3} = 10$ fs from the 1D calculations) see Figure 4.8(a); the field strength is kept at 3.0 GV/m. As shown in Figure 4.8(b), the value of $P_a(\upsilon_{00})$ at the end of the pulse, ~ 0.35, is slightly lower than that of the 1D model, ~ 0.47. Close to the end of the series of half-cycle pulses, at 31.5 fs, the mean displacement of the hydrogen in the 2D model approaches a local maximum value, $q_{as} = 0.197$ Å (Figure 4.8(c)). At a later

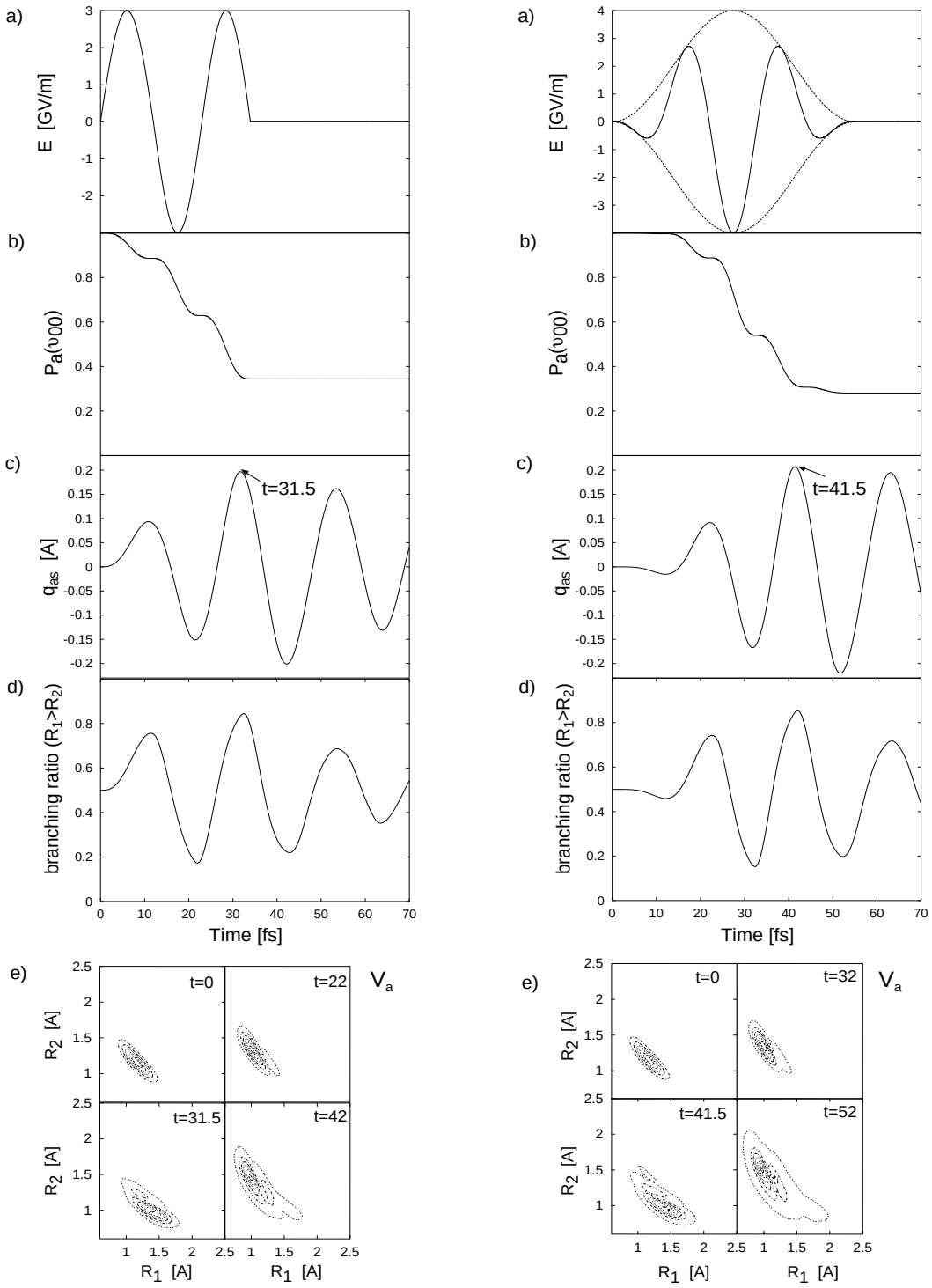

Figure 4.8: Excitation of the vibrational ground state of the 2D model FHF^-. (a) Electric field vs. time. Left panel: Three HCPs, electric field for each HCP given in Eq. (4.7) with following pulse parameters:
$E_{0,1} = 3.0$ GV/m, $t_{0,1} = 0$ fs, and $t_{p1} = 12$ fs;
$E_{0,2} = -3.0$ GV/m, $t_{0,2} = 12$ fs, and $t_{p2} = 11$ fs;
$E_{0,3} = 3.0$ GV/m, $t_{0,3} = 23$ fs, and $t_{p3} = 11$ fs.
Right panel: Electric field given in Eq. (4.8) with pulse parameters $E_0 = -4.0$ GV/m, $\omega_{\mathrm{IR}} = 1516$ cm^{-1}, $\varphi = 0$, $t_0 = 0$ fs, and $t_p = 55$ fs. (b) Population of the vibrational ground state of the anion, given by the modulus of the autocorrelation function, $P_a(\upsilon_{00}) = |\langle \upsilon_{00} | \Psi_a(t > 0) \rangle|^2$. (c) Time evolution of the expectation value of the mean position of the H atom driven by the laser field shown in (a). (d) Branching ratio of species for which $\mathrm{R}_1 > \mathrm{R}_2$ vs. time. (e) Wave functions evolving on V_a at time $t = 0$ fs and times corresponding to the turning points of the oscillation.

time, $t = 42$ fs, $|q_{as}|$ reaches an even larger value of 0.201 Å, a favorable consequence of wave packet dispersion. For times $t > 42$ fs, wave packet dispersion leads to the expected behavior of decreasing mean values of q_{as}. The wave packet remains nonetheless compact during its evolution on the PES of the anion, as shown in Figure 4.8(e) with snapshots of the wave packet at the turning points.

4.3.4 Smooth $\sin^2$ pulse

Finally, the sequence of half-cycle pulses that breaks the symmetry in the 2D system is replaced by a smooth, switch-on-switch-off, $\sin^2$-shaped laser field, as described in Eq. (4.8) and shown in the right panel of Figure 4.8(a). The field strength needs to be increased to $E_{0,\mathrm{IR}} = 4.0$ GV/m to compensate for the slightly diminished outer peak heights. The central carrier energy corresponds to $\omega_{\mathrm{IR}} = 1516$ cm^{-1} and the total pulse duration is $t_{p,\mathrm{IR}} = 55$ fs. From Eq. (2.141), the spectral bandwidth $\Delta\omega$ for a pulse with $t_p = 55$ fs is calculated to be $\Delta\omega > 48$ cm^{-1}, and $\Delta\omega/\omega > 0.03$. The frequency ω corresponds to mean energy spacings between the asymmetric stretching eigenenergies: $\upsilon_{01} \leftarrow \upsilon_{00} = 1448$ cm^{-1} and $\upsilon_{02} \leftarrow \upsilon_{01} = 1697$ cm^{-1}. The phase of the field, φ_{IR}, is set to 0. Note that a shift of π would cause the wave packet initially to be driven in the opposite direction. The mean value of q_{as} reaches 0.207 Å at $t = 41.5$ fs, shown in Figure 4.8(d). The modulus of the autocorrelation function $P_a(\upsilon_{00})$ now drops to 0.28 at $t = 50$ fs due to the high field strength and longer pulse duration. Nonetheless, the wave packet at $t = 41.5$ fs remains relatively compact (Figure 4.8(e)), with a branching ratio of 0.86 at $t = 41.5$ fs (Figure 4.8(d)). Snapshots of the wave packet at maximum displacement are shown in Figure 4.8(e). In other words, at well-defined times, the compact wave packet is localized in bond-specific domains of the PES. To summarize, the effect of the few-cycle IR pulse is to create a superposition of eigenstates—or a compact wave packet—that undergoes dynamical symmetry breaking on the time scale of the period of the asymmetric stretching vibration. Next, we will apply an ultrashort UV pulse to selectively break the pre-excited F–H bond via photoelectron detachment.

4.3.5 Combined IR and UV laser pulses

After the optimized $\sin^2$-shaped few-cycle IR laser pulse has been applied, the wave packet oscillation begins. When the displacement is maximum, 38 fs after the IR pulse is applied, shown in the right of Figure 4.8(a), a resonant $\sin^2$-shaped UV pulse is applied that photodetaches an electron and prepares the system on V_n, the PES of the neutral species. The parameters of the UV pulse are $E_{0,\mathrm{UV}} = 5.0$ GV/m ($I_{\max} = 6.6$ TW/cm^2), $\omega_{\mathrm{UV}} =$

43 548 cm^{-1} ($\equiv$ 5.5 eV), $\varphi_{\mathrm{UV}} = 0$, $t_0 = 38$ fs, and $t_{p,\mathrm{UV}} = 5$ fs. This few-cycle UV pulse excites the displaced wave packet to a bond-selective domain of V_n, causing the wave packet to evolve predominantly along one dissociation channel. Comparison of the right panel of Figure 4.8 and Figure 4.9 shows that the wave packet dynamics of the anion is minimally affected by the presence of the UV pulse due to its relatively low intensity; the neutral state has a $\sim$10% population. Accordingly, non-physical intrapulse pump-dump or competing multiphoton processes are negligible in the present application. This low depletion of the anion ground state is shown in Figure 4.10, in which the curve corresponding to the total population of the anion ground state (norm) begins to drop after $t = 38$ fs, before steadying to $\sim$92%. Figure 4.10 shows the vibrational composition of the wave packet created by the IR pulse, calculated for each vibrational eigenstate from

$$P_{\upsilon} = |\langle \upsilon_{s\,as} | \Psi(t) \rangle|^2. \tag{4.10}$$

At $t = 0$, only υ_{00} is present, as expected for the process starting from the ground state. As the IR pulse is turned on ($t > 0$), the coefficient of υ_{00} drops to 0.08 while the contributions of υ_{01} (asymmetric stretch), υ_{11} (symmetric + asymmetric stretches), and υ_{02} (first excited asymmetric stretch) increase. At $t = 38$ fs, when the UV pulse is applied, the wave packet consists predominantly of the lowest two asymmetric stretching modes υ_{01} ($\sim$0.20) and υ_{02} ($\sim$0.22), and first symmetric-asymmetric mixed-mode, υ_{11} ($\sim$0.11). Contributions from the ground state, υ_{00}, and other low-lying vibrational eigenstates are also present. After a near-vertical FC-type transition, the resulting evolution of the wave packet $\Psi_n(t)$ on the neutral PES (see Figure 4.9(e)) is located in the downward-sloping domain of the neutral PES instead of at the transition state region. Nonetheless, wave packet dispersion allows a small portion of $\Psi_n(t)$ to penetrate the non-desired domain, $R_2 > R_1$, such that the initial branching ratio of $\sim$0.85 at $t = 42$ fs drops to $\sim$0.75 at $t = 70$ fs. At $t = 70$ fs, the branching ratio (F + HF:FH + F) is increased from its natural value of 0.5 : 0.5 to 0.75 : 0.25 (see Figure 4.9(d)). As soon as $\Psi_n(t)$ reaches the near-asymptotic domain of V_n (for which R_1 is larger than $\sim$ 2 Å), the high potential ridge hinders further penetration of the dispersed wave packet, such that $\Psi_n(t)$ dissociates preferably along the selected bond R_1. The small oscillations in the branching ratio for times $t > 42$ fs are due to small coherent vibrational excitations of the product F + FH, a phenomenon that has been observed in other systems as well [159, 160].

4.3.6 Isotope effects: dynamics of FDF$^-$

In Section 3.2, the isotopomer FDF$^-$ was discussed and a scaling factor b was introduced that described the ratio of the asymmetric stretching frequencies, $\nu_3(\mathrm{FHF}^-)/\nu_3(\mathrm{FDF}^-) = 1.45$. Using this information, we can re-optimize the IR

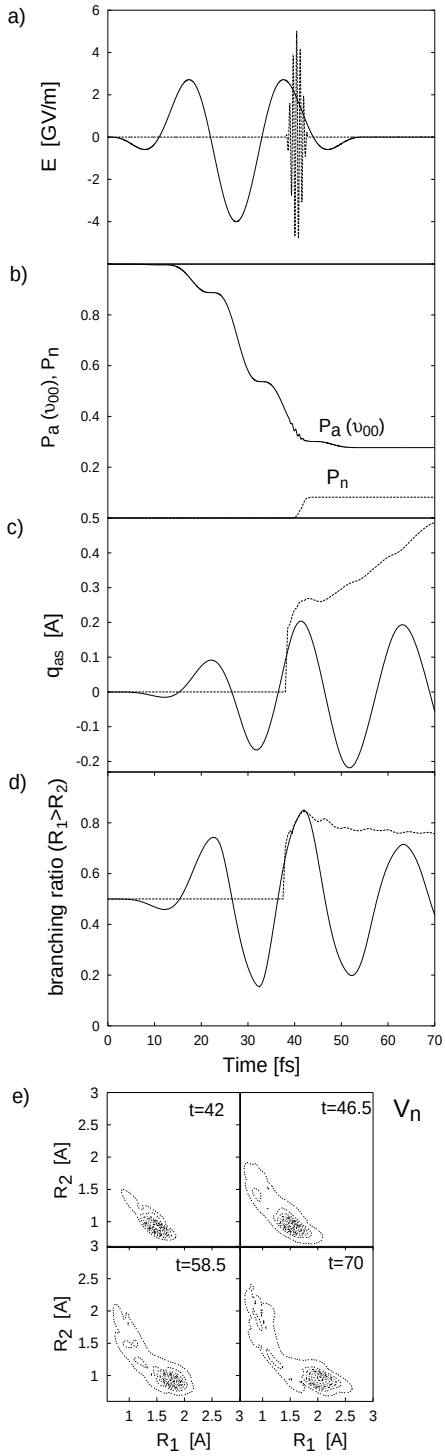

Figure 4.9: Excitation of the vibrational ground state of the 2D model FHF^-, using a few-cycle $\sin^2$-shaped IR pulse (solid), followed by an ultrashort $\sin^2$-shaped UV pulse (dotted). (a) Electric field vs. time. IR and UV electric fields given by Eq. (4.8). IR pulse parameters: $E_{0,\mathrm{IR}} = -4.0$ GV/m, $\omega_{\mathrm{IR}} = 1516$ cm^{-1}, $\varphi_{\mathrm{IR}} = 0$, $t_{0,\mathrm{IR}} = 0$ fs, and $t_{p,\mathrm{IR}} = 55$ fs. UV pulse parameters: $E_{0,\mathrm{UV}} = 5.0$ GV/m, $\omega_{\mathrm{UV}} = 43\,548$ cm^{-1}, $\varphi_{\mathrm{UV}} = 0$, $t_{0,\mathrm{UV}} = 38$ fs, and $t_{p,\mathrm{UV}} = 5$ fs. (b) Population of the vibrational ground state of the anion, given by the modulus of the autocorrelation function, $P_a(\upsilon_{00}) = |\langle \upsilon_{00}|\Psi_a(t > 0)\rangle|^2$ (solid), and population of the neutral state, P_n (dotted). (c) Time evolution of the expectation value of the mean position of the H atom in the anion (solid) and neutral (dotted) driven by the laser field shown in (a). (d) Branching ratio of species for which $R_1 > R_2$ vs. time. (e) Wave functions evolving on V_n at time $t = 42$ fs and for later times $t > 42$ fs.

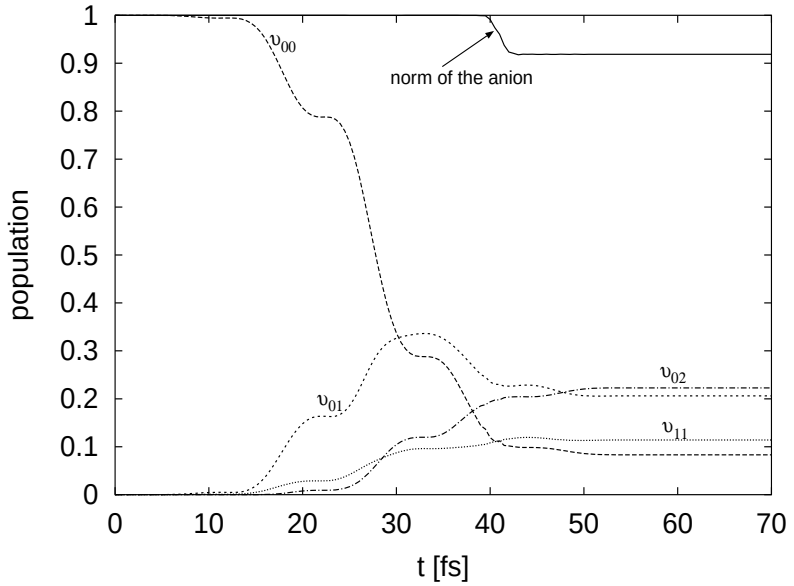

Figure 4.10: Generation of a vibrational wave packet from a few-cycle IR pulse, given in Eq. (4.8). The pulse parameters are $E_{0,\mathrm{IR}} = -4.0$ GV/m, $\omega_{\mathrm{IR}} = 1516$ cm^{-1}, $\varphi_{\mathrm{IR}} = 0$, $t_{0,\mathrm{IR}} = 0$ fs, and $t_{p,\mathrm{IR}} = 55$ fs. Dominant contributions are from vibrational eigenstates v_{00}, v_{01} (asymmetric stretch), v_{11} (symmetric + asymmetric), and v_{02} (first excited asymmetric stretch). Depletion of population (norm) in the anion (FHF^-) ground state begins at $t = 38$ fs, when the UV pulse is fired. Pulse parameters are $E_{0,\mathrm{UV}} = 5.0$ GV/m, $\omega_{\mathrm{UV}} = 43\,548$ cm^{-1}, $\varphi_{\mathrm{IR}} = 0$, $t_{0,\mathrm{UV}} = 38$ fs, and $t_{p,\mathrm{UV}} = 5$ fs (see Figure 4.9(a)). After vertical excitation of population to the neutral FHF state, anion population (norm) drops to ~ 0.92.

pulse that was used to achieve dynamical symmetry breaking in FHF^-, such that it achieves similar symmetry breaking in the heavier isotopomer, FDF^-. The parameters that need to be changed are the IR frequency, ω_{IR} and the IR pulse duration, $t_{p,\mathrm{IR}}$, since these values determine the timing of the IR cycles that drive the asymmetric stretching vibration. Also, the delay between the IR and UV pulses must be adjusted for the longer IR pulse. The results of this simulation are shown in Figure 4.11.

The parameters of the laser pulses shown in Figure 4.11(a) are $E_{0,\mathrm{IR}} = 4.0$ GV/m ($I_{\max} = 4.2$ TW/cm^2), $\omega_{\mathrm{IR}} = 992$ cm^{-1}, $\varphi_{\mathrm{IR}} = 0$, $t_0 = 0$ fs, and $t_{p,\mathrm{IR}} = 84$ fs. After a delay of 46 fs, *i.e.* $t_{0,\mathrm{UV}} = 46$ fs, the UV pulse is fired. Since the vertical spacing between V_a and V_n is identical for $\mathrm{FDF}^-/\mathrm{FDF}$ compared to that of $\mathrm{FHF}^-/\mathrm{FHF}$, the remaining parameters of the UV pulse are identical to those used in the case of FHF^-: $E_{0,\mathrm{UV}} = 5.0$ GV/m ($I_{\max} = 6.6$ TW/cm^2), $\omega_{\mathrm{UV}} = 43\,548$ cm^{-1} ($\equiv 5.5$ eV), $\varphi_{UV} = 0$, and $t_{p,\mathrm{UV}} = 5$ fs. The frequency of the IR pulse ω_{IR}, as well as the pulse duration, $t_{p,\mathrm{IR}}$, were scaled according to the isotope factor $b = 1.45$, to account for the heavier mass of deuterium, and then slightly optimized. Accordingly, the ratios $t_{p,\mathrm{IR}}\mathrm{FDF}^-/t_{p,\mathrm{IR}}\mathrm{FHF}^- = 84/55 = 1.52$ and $\omega_{\mathrm{IR}}\mathrm{FDF}^-/\omega_{\mathrm{IR}}\mathrm{FHF}^- = 1516/992 = 1.53$, are close to the value of b. The total propagation time is 100 fs, a longer propagation time than in the FHF^- case, since the dynamics are slower for the heavier species. A maximum mean extension of the F–D bond from its

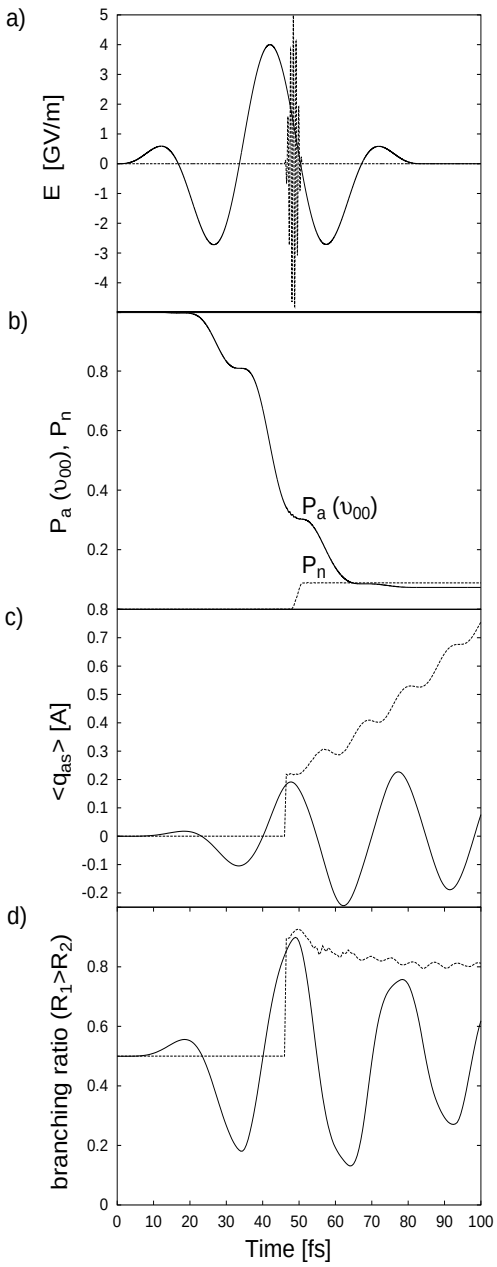

Figure 4.11: Excitation of the vibrational ground state of the 2D model FDF$^-$, using a few-cycle sin^2-shaped IR pulse (solid), followed by an ultrashort sin^2-shaped UV pulse (dotted). (a) Electric field vs. time; IR and UV electric fields given by Eq. (4.8). The parameters of the IR laser pulse are re-tuned from those of FHF$^-$ (*cf.* Figure 4.9) according to the scaling factor, $b=1.45$ and are $E_{0,\mathrm{IR}}=-4.0$ GV/m, $\omega_{\mathrm{IR}}=992$ cm^{-1}, $\varphi_{\mathrm{IR}}=0$, $t_{0,\mathrm{IR}}=0$ fs, and $t_{p,\mathrm{IR}}=84$ fs. UV pulse parameters: $E_{0,\mathrm{UV}}=5.0$ GV/m, $\omega_{\mathrm{UV}}=43\,548$ cm^{-1}, $\varphi_{\mathrm{UV}}=0$, $t_{0,\mathrm{UV}}=46$ fs, and $t_{p,\mathrm{UV}}=5$ fs. (b) Population of the vibrational ground state of the anion, given by the modulus of the autocorrelation function, $P_a(\upsilon_{00})=|\langle\upsilon_{00}|\Psi_a(t>0)\rangle|^2$ (solid), and population of the neutral state, P_n (dotted). (c) Time evolution of the expectation value of the mean position of the H atom in the anion (solid) and neutral (dotted) driven by the laser field shown in (a). (d) Branching ratio of species for which $\mathrm{R}_1>\mathrm{R}_2$ vs. time.

initial value, 1.16 Å, to 1.31 Å, is observed at 48.5 fs (compare with 42 fs for FHF$^-$). Slightly before this time, at 46 fs, the UV pulse is fired such that the wave packet is

localized at the turning point of its oscillation for most of the UV pulse duration. The mean value of the asymmetric stretch at 48.5 fs is $q_{as} = 0.15$ Å, and the localization of the wave function in the domain $R_1 > R_2$ of the products FD + F reaches 0.85, before decreasing slightly to ~ 0.80. In other words, after scaling the parameters of the few-cycle IR laser pulse, the natural branching ratio of $0.50 : 0.50$ was increased to $0.80 : 0.20$, a slightly higher branching ratio than that found in the case of FHF ($0.75 : 0.25$).

The present combined few-cycle IR + UV laser pulses achieve symmetry breaking in the electronic ground state of the anion and subsequent selective bond breaking of the neutral system to enhance the natural branching ratio of FHF and FDF from $0.50 : 0.50$ to $0.75 : 0.25$ and $0.80 : 0.20$, respectively. In these wave packet simulations, the molecular axis of the anion is assumed to be optimally aligned, such that the body-fixed z axis is parallel to the space-fixed Z electric field vector. This assumption implies that the efficiency of the IR and UV laser pulses is maximum. The IR laser field stretches the aligned bond, and the subsequent UV laser pulse dissociates the pre-excited bond, driving the atomic and molecular products in opposite ($+Z$ and $-Z$) directions, thereby giving rise to a spatial separation of products. In the next section, we will discuss how the results of these wave packet simulations change if this assumed molecular alignment no longer exists.

4.3.7 Spatial distribution of products

Figure 4.12 presents a schematic depiction of the anion FHF^- in a space-fixed frame of reference, such that the molecular z axis of the anion is parallel to the space-fixed Z axis, and the angle θ between the two axes is zero, $\theta = 0°$. Furthermore, the two fluorine atoms, F_A and F_B, are considered distinguishable, such that F_A lies in the $+Z$ direction and F_B is pointed toward $-Z$; for the case in which F_A lies in the $-Z$ direction, $\theta = 180°$. The

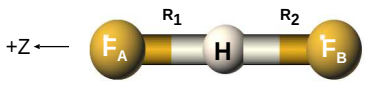

Figure 4.12: Schematic representation of oriented FHF^- with F_A in direction $+Z$, and the angle θ between the molecular axis and space-fixed Z axis is zero.

dissociation products that can be obtained are (F_A + HF_B) for $R_1 > R_2$ and (F_AH + F_B) for $R_2 > R_1$. In this section, we are not attempting to *control* molecular orientation but rather first to characterize the role it plays in our IR + UV pulse simulations. Specifically, for an ensemble of randomly oriented molecules, we will examine the product yields

(F_A + HF_B) versus (F_AH + F_B) as a function of molecular orientation.[2] In the previous section, for an assumed optimal orientation ($\theta = 0°$), a branching ratio of $\sim 0.75:0.25$ was obtained for the dissociation products (F_A + HF_B) versus (F_AH + F_B). Now, we will examine the branching ratio of neutral products for various molecular orientations, *i.e.* for $\pm$ values of θ. Furthermore, we will show that for molecular orientation along the laser polarization axis, the laser-driven dissociation reaction leads to a spatial distribution of dissociation fragments. Later, in Section 4.4.1, we will design an IR pulse that manipulates the orientation of the system before subsequent IR + UV control pulses are applied.

Let us begin the discussion by considering the anion FHF^- that is assumed to be oriented in the $+Z$ space-fixed axis, along which the IR and UV laser pulses are also linearly polarized. For this situation of optimal molecular orientation ($\theta = 0°$), the parameters of the IR and UV laser pulses are tuned to achieve maximum bond extension and a maximum branching ratio of (F_A + HF_B):(F_AH + F_B). To understand the origin of orientation effects, it is instructive to review the time-dependent potential for the anionic species (see Eq. (4.2)), recast in the following form:

$$\hat{\mathbf{V}}_a(t) = \hat{\mathbf{V}}_a - E(t)\,\cos\theta\,\mu_a. \tag{4.11}$$

The factor $\cos\theta$ determines the overlap of the electric field vector and the dipole moment. Obviously, increasing θ from 0° to 90° will decrease $\cos\theta$ from 1 to 0; the same trend will be observed for increasing θ from 90° to 180°. In previous simulations, θ was set to 0°; now, we will examine the response of the wave packet dynamics for values of $\theta \neq 0°$, namely for two extreme cases, $\theta = 10°$ and $\theta = 80°$, close to parallel and perpendicular orientations of the anion relative to laser polarizations, respectively. Due to the symmetry of the system, equivalent results are obtained for the corresponding angles 180°–10° and 180°−80°, or in general for $\theta' = 180° - \theta$. One can anticipate that the spatial distribution of dissociation products of an asymmetric systems (XHY^-), will *not* be equivalent for molecules of opposite orientations. The results of wave packet simulations for the cases $\theta = 10°$ and $\theta = 80°$ in FHF^- are presented in Figure 4.13. The electric field, shown in Figure 4.13(a), consists of the IR pulse (solid) and the UV pulse (dotted). As expected, the left panel, corresponding to an orientation close to optimal laser interaction ($\theta = 10°$), demonstrates almost no decrease in the field signal. For the case $\theta = 80°$, the field is significantly attenuated; the resulting wave packet dynamics (Figure 4.13(b-d), right panel) reflect this effective low field strength. The diminished effective field interacts minimally with the dipole of the anion and weakly excites the asymmetric stretching vibration. The field is ineffective at driving the asymmetric stretching vibration and as a result, the mean amplitudes of the asymmetric stretch, q_{as}, are significantly smaller for

[2] In reality, since FHF^- is symmetric under inversion, one can only speak of its *alignment* since head can not be distinguished from tail.

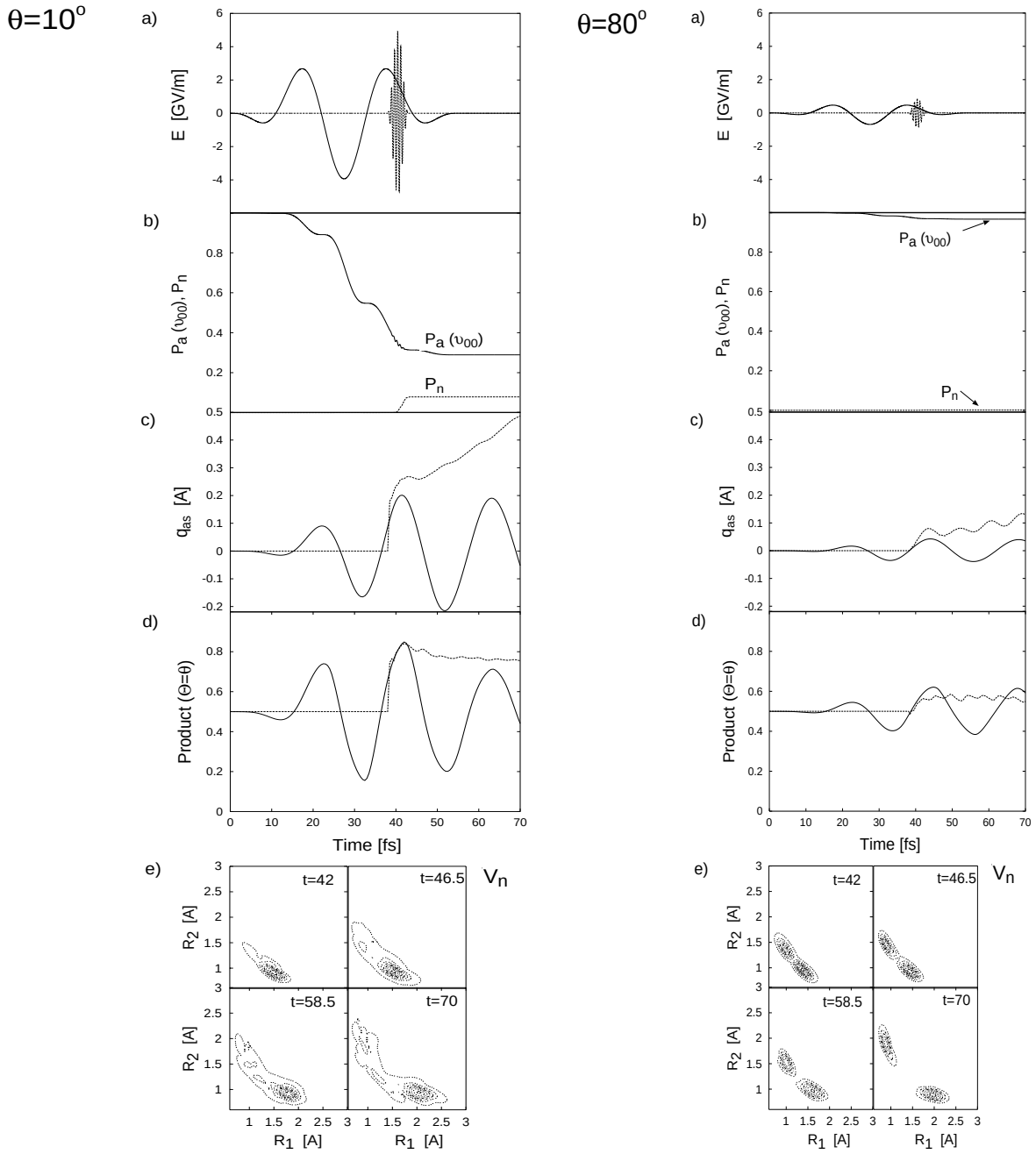

Figure 4.13: Effects of linearly-(Z)-polarized IR (solid line) and UV (dotted line) laser pulses on the collinear reactant FHF^- with orientation $\theta = 10°$ (left panels) and $\theta = 80°$ (right panels). (a) Few-cycle IR + UV laser fields $E(t)\cos\theta$ as seen by reactants at angles θ; $E(t)$ for IR and UV electric fields given by Eq. (4.8). IR pulse parameters: $E_{0,\mathrm{IR}} = -4.0$ GV/m, $\omega_{\mathrm{IR}} = 1516$ cm^{-1}, $\varphi_{\mathrm{IR}} = 0$, $t_{0,\mathrm{IR}} = 0$ fs, and $t_{p,\mathrm{IR}} = 55$ fs. UV pulse parameters: $E_{0,\mathrm{UV}} = 5.0$ GV/m, $\omega_{\mathrm{UV}} = 43\,548$ cm^{-1}, $\varphi_{\mathrm{UV}} = 0$, $t_{0,\mathrm{UV}} = 38$ fs, and $t_{p,\mathrm{UV}} = 5$ fs. (b) Population of the anion in the ground vibrational state, $P_a(\upsilon_{00}) = |\langle\upsilon_{00}|\Psi_a(t > 0)\rangle|^2$ (solid), and neutral, P_n (dotted), systems. (c) Mean value of the asymmetric stretching coordinate q_{as} for the anion (solid lines) and neutral system (dotted lines). (d) Branching ratio of the anion (solid line) and the neutral system (dotted line) in the domain in which $R_1 > R_2$. The corresponding molecular fragments are scattered in the direction Θ of the initial orientation θ. (e) Snapshots of resulting wave packet evolution on neutral surface V_n. Contours are shown with lines of equidensity, but are renormalized for each case; the integrated densities yield probabilities $P_n = 0.079$ and $P_n = 0.001$ for the different orientations, $\theta = 10°$ and 80°, respectively.

the anion (solid), shown in Figure 4.13(c). Furthermore, for the previous case of perfect orientation ($\theta = 0°$), the frequency of the UV pulse had been tuned to the energy gap between the neutral and anionic potential energy surfaces,

$$\omega_{\mathrm{UV}} = \frac{\mathrm{V}_n - \mathrm{V}_a}{\hbar}. \tag{4.12}$$

at the geometry corresponding to the optimally extended and compressed bonds R_1 and R_2, respectively. Now, for $\theta \neq 0°$, this geometry is never realized and the frequency is off-resonant; the pulse no longer efficiently transfers population to the neutral surface and the probability of photodetachment decreases to almost zero for values of $\theta \to 90°$; the population P_n grows minimally (Figure 4.13(b)). Marginal probabilities of photodetachment remain for $\theta = 90°$ due to the frequency bandwidth, $\Delta\omega_{\mathrm{UV}} = 565\ \mathrm{cm}^{-1}$, of the ultrashort 5 fs UV pulse that arises from the uncertainty relationship $\Delta t_p \Delta\omega \geq 1/2$ (see Eq. (2.141)). The mean amplitudes of the asymmetric stretch, q_{as}, in the neutral system (Figure 4.13(c), dotted line) are accordingly greatly reduced. Furthermore, because the extensions and compressions of the two bonds, R_1 and R_2, are smaller, the resulting branching ratios $P_a(v_{00})$ of the anion (solid) and P_n of the neutral (dotted) hover near 0.5 (Figure 4.13(d)), since the wave packet has not been asymmetrically displaced from the equilibrium position. Snapshots of the evolution of the wave packet on the neutral potential energy surface, V_n for the cases $\theta = 10°$ and $\theta = 80°$ are shown in Figure 4.13(e).

On the left ($\theta = 10°$), the integrated equidensity contours yield probabilities $P_n = 0.079$ whereas on the right ($\theta = 80°$), the total density is $P_n = 0.001$. The near-vertical Franck-Condon-type transition implies that the neutral wave packet is prepared with essentially the same asymmetry as the anionic one. In the case of near parallel alignment ($\theta = 10°$), the IR pulse is still effective in initiating dynamic symmetry breaking in the anionic system, such that R_1 and R_2 are stretched and compressed, and a wave packet is created that is displaced from the equilibrium position. Upon vertical excitation by the UV pulse, this wave packet is prepared predominantly in the region $\mathrm{R}_1 > \mathrm{R}_2$, such that the Product($\Theta = \theta$) = 0.75 : 0.25 is obtained. In the case of unfavorable orientation, $\theta = 80°$, the IR pulse is ineffective in obtaining dynamical symmetry breaking, so the excitation of the wave packet to the neutral PES is to a region in which $\mathrm{R}_1 \approx \mathrm{R}_2$ and almost equal—albeit small—wave packet densities exist in both dissociation channels, and Product($\Theta = \theta$) $\approx$ 0.50 : 0.50.

Wave packet dynamics have been shown for two specific cases, namely $\theta = 10°$ and $\theta = 80°$, but the behavior can be expanded to a range of orientation angles—θ increasing from 0° to 180°. Figure 4.14 shows these trends. Figure 4.14(a) plots P_n, the probability of observing the neutral system FHF; Figure 4.14(b) shows $P(\Theta, \mathrm{HF})$, the probability of observing the molecular product $\mathrm{F}_A\mathrm{H}$ dissociate in the direction Θ;

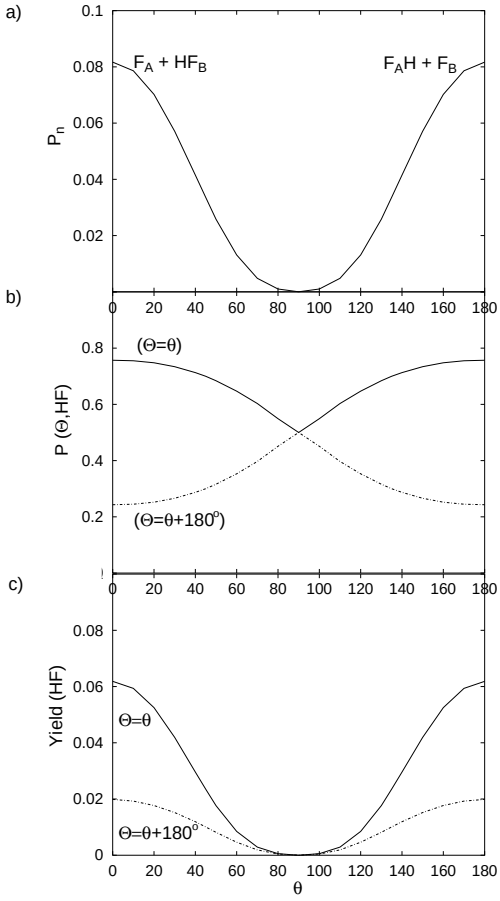

Figure 4.14: Spatial localization of dissociation products after few-cycle IR + UV laser pulses, given by $E(t)\cos\theta$, where θ is the angle between the reactant FHF^- and the linearly polarized laser fields. $E(t)$ for IR and UV electric fields given by Eq. (4.8). IR pulse parameters: $E_{0,\mathrm{IR}} = -4.0$ GV/m, $\omega_{\mathrm{IR}} = 1516$ cm^{-1}, $\varphi_{\mathrm{IR}} = 0$, $t_{0,\mathrm{IR}} = 0$ fs, and $t_{p,\mathrm{IR}} = 55$ fs. UV pulse parameters: $E_{0,\mathrm{UV}} = 5.0$ GV/m, $\omega_{\mathrm{UV}} = 43\,548$ cm^{-1}, $\varphi_{\mathrm{UV}} = 0$, $t_{0,\mathrm{UV}} = 38$ fs, and $t_{p,\mathrm{UV}} = 5$ fs.
(a) Probability P_n of observing the neutral system. (b) Probability $P(\Theta, \mathrm{FH})$ of observing the molecular product HF dissociate in the direction Θ. (c) The product yield $Y(\mathrm{FH}) = P_n \cdot P(\Theta, \mathrm{FH})$ versus the orientation angle θ between the reactant FHF^- and the linearly (Z) polarized IR + UV laser pulses. An alternate representation of the yield is given in Figure 4.15 as a polar diagram.

Figure 4.14(c) depicts $Y(\mathrm{FH})$, the total product yield of F_AH, defined as

$$Y(\mathrm{FH}) = P_n \cdot P(\Theta, \mathrm{FH}). \tag{4.13}$$

In other words, the quantity P_n is an indication of how effective the UV laser pulse is at photodetaching an electron and preparing the neutral system. $P(\Theta, \mathrm{FH})$ is an orientation-dependent branching ratio; for perfect orientation ($\Theta = \theta = 0°$ or $\theta = 180°$), the molecular FH and atomic F fragments will dissociate in opposite directions with maximum probability $P(\Theta, \mathrm{FH})$, thus spatially separating the products. For our model system F_AHF_B, this separation distinguishes between (F_A + HF_B) and (F_BH + F_B), although in an experiment, these products are chemically equivalent and no distinction could be made. For $\theta = 90°$, $P(\Theta, \mathrm{FH})$ is expected to be 0.5 since both products are

present in equal amounts. The yield, $Y(\mathrm{FH})$, is the amount of neutral species created times the branching ratio of $(F_AH + F_B)$:$(F_A + HF_B)$. The spatial localization of the yield of products HF is shown in Figure 4.15 as a polar diagram. For perfect orientation ($\theta = 0°$), $Y(F_AH)$ is maximum, with molecular products F_AH and atomic products F_B scattered toward $\Theta = \theta$ and $\Theta = \theta + 180°$, respectively. For perpendicular orientations, $Y(\mathrm{FH})$ drops to zero since the field's interaction with the anion is negligible.

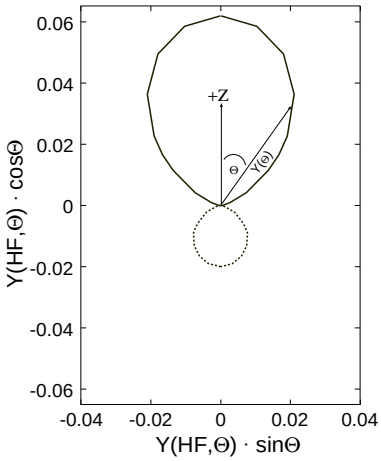

Figure 4.15: Polar diagram of the yield $Y(\mathrm{FH}) = P_n \cdot P(\Theta, \mathrm{FH})$ of molecular products F_AH, scattered preferentially to $\Theta = \theta$ (big solid lobe in direction $+Z$), and atomic products F_B, scattered preferentially toward $\Theta = \theta + 180°$ (small dashed lobe in direction $-Z$).

To summarize, in an ensemble of randomly positioned molecules, the efficiency of the IR laser in exciting a specific bond is greatly reduced. The subsequent UV laser pulse therefore has a greatly reduced chance of exciting the anion system to a bond-selective region of the neutral PES and producing a desired chemical product. For our model system, F_AHF_B, a high yield of products is obtained for orientations near $\theta = 0°$ or $\theta = 180°$. Molecules lying perpendicular to the field ($\theta = 90°$) will interact negligibly with the field; the yield of products will be close to zero, and the branching ratio $(F_AH + F_B)$:$(F_A + HF_B)$ will be nearly 0.50 : 0.50. Nonethless, as shown in Figure 4.15, atomic and molecular dissociation products F + HF can be separated spatially along the directions $\theta = 0°$ and $\theta = 180°$, respectively. Although the distinction made here between the products $(F_A + HF_B)$ and $(F_AH + F_B)$ is purely abstract, atomic and molecule dissociation products F + HF will be separated spatially along the directions $\theta = 0°$ and $\theta = 180°$, respectively, as shown in Figure 4.15. In the next chapter, molecular orientation will be treated explicitly for the asymmetric system OHF^-.

4.4 Results for OHF^-/OHF

The quantum dynamical results of the second model system, OHF^-, will be presented in this section. The first part of this section will focus on controlling the orientation of the asymmetric linear molecule OHF^- using a linearly polarized, IR half-cycle pulse (HCP). In the second part of the discussion, few-cycle IR and UV laser pulses will be applied to the *pre-oriented* model system, in which the body-fixed $+z$ axis of the molecule will be assumed to be oriented in the space-fixed $+Z$ direction, such that the angle θ between the molecular axis of OHF^- and $+Z$ is 0. This relative orientation of the molecular axis of OHF^- with respect to the space-fixed coordinate system is shown in Figure 4.16.

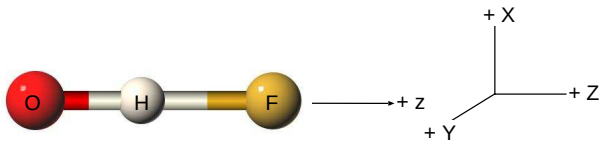

Figure 4.16: Relative orientation of the body-fixed z axis of OHF^- with respect to the space-fixed coordinate system XYZ

Time-dependent wave packet propagations were calculated with the split-operator method [138, 139], using a time step $\Delta t = 0.01$ fs. The 2D model consisted of the bond distances $R_1 = R_{OH}$ and $R_2 = R_{HF}$, which ranged from 0.6 to 4.0 Å and from 0.6 to 5.0 Å, respectively. The discretized grids of the anion and neutral PESs, as well as the anionic permanent dipole surface, consisted each of $\mathcal{N} = 64 \times 64 = 4096$ bi-cubically splined points [158]. Branching ratios of the neutral dissociative system were obtained by summing the normalized population density $|\Psi_n(R_1, R_2, t)|^2$ over the grid halves, $R_1 > R_2$ and $R_2 > R_1$.

To absorb wave packet fluxes at the boundary of the grid, a gobbler function was used, as implemented in the program *qmpropa* [141]. The gobbler parameter, defined in Eqs. (2.157) and (2.159), was set to $g = 2$, such that the exponential factor is $g_0 = 2.3$.

4.4.1 Half-cycle pulses (HCP) to control molecular orientation

In Section 4.3.7, the dependence of product yields on the relative orientation of reactants in the laser field was examined. For near-parallel alignments of FHF^- in the laser field, a maximum yield was obtained, whereas for perpendicular alignments, the yield was negligible. In this section, we present results obtained from the *active* orientation of

OHF^- using an infrared HCP. For these simulations, we consider our linear triatomic molecule to be rigid (not vibrating), and to be in the vibrational ground state (υ_{00}) as well as in the electronic ground state, $^2\Pi$. The electronic orbital angular momentum and spin quantum numbers corresponding to this state are $L=1$ and $S=\frac{1}{2}$, respectively. For our simulations, however, the spin angular momentum will be neglected for computational simplicity, although its contribution should formally be considered. Therefore, in the zero temperature case ($T=0$ K), at $t=0$, we will set $J=R+L+S=1$ (see Eq. (2.201)). Next, our rigid molecule is subjected to a linearly (Z) polarized HCP, as introduced in Section 2.5.3,

$$\vec{E}(t) = \vec{\varepsilon}_Z E_0 \cos(\omega\, t + \varphi) \cdot s(t) \tag{4.14}$$

where the envelope function is the Gaussian centered at time $t=t_0$,

$$s(t) = e^{-(t-t_0)^2/\sigma^2}. \tag{4.15}$$

E_0 is the field amplitude, and the pulse width parameter $\sigma = 279$ fs is short compared to the rotational period, $\sigma \leq \pi\hbar/B = 49.6$ ps. In this limit, the field-matter interaction is nonadiabatic and rotational wave packets are generated. The pulse duration is chosen to include one half-cycle of the oscillation, which has a frequency, ω, centered in these applications at $\omega = 36$ cm^{-1} (1 THz). The IR frequency, ω, is an off-resonant frequency that induces essentially no vibrations. In fact, the pulse frequency used in these simulations is much larger than the spacing between the low-lying rotational energy levels of OHF^-, $2B$, $4B$, $6B, \ldots$, for $B=0.33$ cm^{-1} (see Table 3.8).

The field-matter interaction, introduced in Eq. (2.228) (see Section 2.5.3), is given as

$$-\vec{\boldsymbol{\mu}} \cdot \vec{E}(t) = -\mu_0\, E(t) \cos\,\theta,$$

where θ is the angle between the body-fixed z axis and the space-fixed Z axis. The molecule-plus-field Hamiltonian for this model is therefore

$$\hat{\mathbf{H}} = B\hat{\mathbf{J}}^2 - \mu_0\, E(t) \cos\,\theta. \tag{4.16}$$

The permanent electric dipole moment μ_0 is calculated from $\langle \upsilon_{00}|\vec{\boldsymbol{\mu}}|\upsilon_{00}\rangle = \mu_0$, where υ_{00} is the ground state anharmonic vibrational wave function calculated at the UMP4 level of theory. At the equilibrium geometry, $R_{OH}=1.07$ Å and $R_{HF}=1.38$ Å, the permanent dipole moment is calculated to be $\mu_0=1.05$ D. The expectation value of $\cos\,\theta$ is used as the orientation paramenter, and it is time and temperature dependent, $\langle \cos\,\theta\rangle_T(t)$, as described in Eq. (2.236). For large positive or negative values of $\langle \cos\,\theta\rangle_T(t)$, orientation in the $+Z$ (or $-Z$) direction is high.

The rigid rotor wave function that is used in the numerical simulations was defined in Section 2.5, in Eq. (2.220). For the calculation of $3-J$ symbols, a numerical

routine, adapted from Refs. [142, 145], is implemented into our program [161] that incorporates an ordinary differential equation solver [158]. A total of forty J states are included in the wave packet propagations. The value of Ω, the projection of L on the body-fixed z axis, remains 1 throughout all simulations, so Ω will not be specified further in the subsequent notation. In the zero temperature case ($T = 0$ K), the value of M at $t = 0$ is assumed to be 0, and this value is conserved throughout the propagation. This treatment is an approximation; an exact treatment would include initial M states equal to -1, 0, and 1 due to the possible projections of $J = 1$ onto the space-fixed Z-axis. For non-zero temperature cases, an incoherent summation over initial J_i and corresponding M_i states is performed. For three temperature cases, $T = 5$, 10, and 20 K, initial J_i states are considered for which the Boltzmann population is greater than 10^{-6}. For $T = 5$, 10, and 20 K, the initial J_i states considered in the propagation are $J_i = 1, .., 11$, $J_i = 1, .., 16$, and $J_i = 1, .., 23$, respectively. The values of M_i accordingly vary from $-J_i$ to J_i. The orientation observable $\langle \cos\theta \rangle$ is calculated in the zero temperature case according Eq. (2.235), and in the case of thermal averaging, the orientation cosine is weighted with the appropriate Boltzmann factors according to Eq. (2.236).

In the first application, a HCP (with the form given in Eq. (4.14)) is applied to OHF^- with the following parameters: $\omega = 36$ cm^{-1}, $\varphi = 0$, $t_0 = 1.0$ ps, and $\sigma = 279$ fs. We will examine the resulting wave packet dynamics first for an intermediate intensity, $I = 4 \times 10^8$ W/cm^2, and a rotationally cold sample, $T = 0$ K. In the subsequent simulations, we will consider varying intensities and temperatures. At time $t = 0$, the angular momentum due to the orbiting rigid body is $R = 0$, and 100% of the population is in the state $J = 1$, $|C^{J=1\,\Omega\,M}|^2 = 1$ as seen in Figure 4.17, for a plot of time-dependent rotational eigenstate coefficients, $|C^{J\,\Omega\,M}|^2$ versus time; the laser pulse is superimposed (dotted line) on the plot. Furthermore, at $t=0$, the molecule is nearly randomly oriented with respect to the laser field, and $\langle \cos\theta \rangle(t) \approx 0$, as shown in Figure 4.18.[3]

As the laser is turned on, the system exchanges units of angular momentum with the external field. In the presence of linearly polarized light, the projection ($M\hbar$) of the total angular momentum (J) along the space-fixed Z axis is conserved, $\Delta M = 0$, while $\Delta J = \pm 1$. Population begins to migrate out of the state $J = 1$ and into other low-lying rotational states, creating a superposition of rotational states, or a rotational wave packet. After the field has been removed, the wave packet consists of $|C^{J=1\,\Omega\,M}|^2 \approx 0.82$, $|C^{J=2\,\Omega\,M}|^2 \approx 0.16$, with minor contributions from $J = 3$ and $J = 4$ states, shown in Figure 4.17. The orientation cosine, $\langle \cos\theta \rangle(t)$, is plotted versus time in Figure 4.18.

[3]Due to the initial rotational state of the molecule, $J = 1$ and $M = 0$, the initial angular distribution about the space-fixed Z axis is not spherically symmetric but rather demonstrates bi-lobal symmetry, such that a perfectly isotropic distribution of the wave function, $\langle \cos\theta \rangle(t) = 0$, is not obtained.

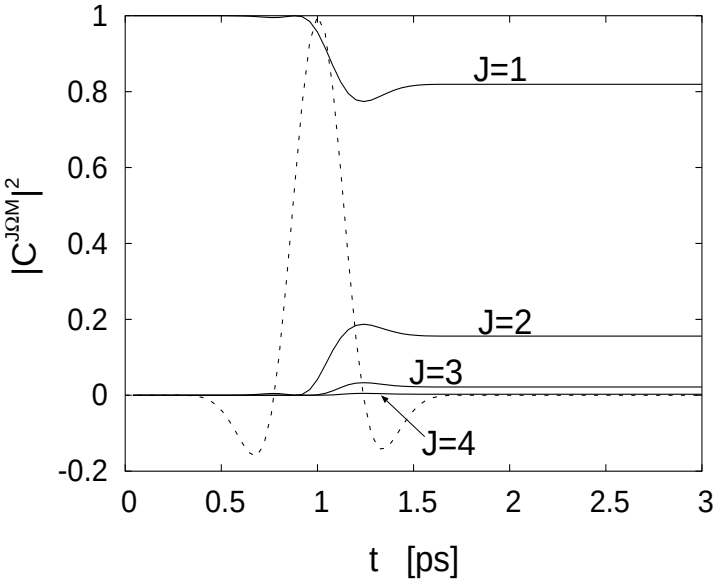

Figure 4.17: Change in population of rotational levels at $T = 0$ K, starting from $|C^{J=1\,\Omega\,M}|^2 = 1$, in OHF^-, with a HCP superimposed (dotted line) on rotational levels. Pulse parameters are $I = 4 \times 10^8$ W/cm^2, $\omega = 36$ cm^{-1}, $\varphi = 0$, $t_0 = 1.0$ ps, and $\sigma = 279$ fs.

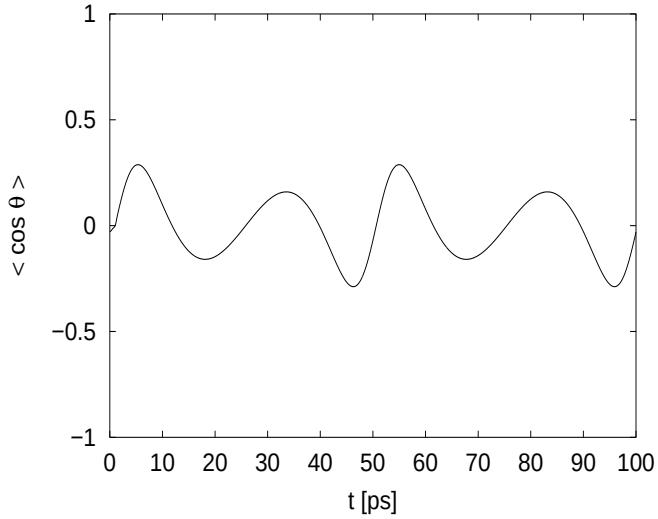

Figure 4.18: Orientation parameter $\langle \cos\theta \rangle_T(t)$ at $T = 0$ K after a HCP ($I = 4 \times 10^8$ W/cm^2), starting from $J = 1$, in OHF^-. Pulse parameters are the same as those described in Figure 4.17.

The oscillations follow basically a two-level ($J = 1$ and $J = 2$) beat pattern that mirrors the flux of population between these two levels. Slight deviations from a pure sinusoidal curve are apparent, due to small populations in higher-lying J states which contribute different phase factors to the time-dependent coefficients (see Eq. (2.229)). Rotational revivals are also present, where the periodicity of the oscillation pattern is determined by

the rotational period of the system OHF^-,

$$\tau_{\text{revival}} = \frac{\pi\hbar}{B}, \tag{4.17}$$

where B is the rotational constant, which for OHF^- is 0.33 cm^{-1}. The revival period is therefore 49.6 ps, as clearly observed in Figure 4.18. One should note that the rotational revivals persist under field-free conditions, *i.e.* the field is turned off for times $t > 2$ ps but revivals are present for the entire propagation period, and they recur as long as coherence in the wave packet is maintained. Next, we will examine rotational wave packet dynamics for different field strengths (intensities) and temperatures.

Intensity dependence

For a given temperature, higher field strengths lead to the population of more rotational levels and to a higher degree of orientation. Figure 4.19(a), (b), and (c) shows the wave packet composition for three different intensities, 2, 4, and 8×10^8 W/cm^2, respectively, at $T = 0$ K. Population in the initial state, $J = 1$, slowly migrates into higher-lying J states while the field is on, with the biggest change in population observed following the maximum field strength, shortly after $t = 1$ ps.

For the lowest intensity, $I = 2 \times 10^8$ W/cm^2 (Figure 4.19(a)), $|C^{J=1\,\Omega\,M}|^2$ drops to 0.90 while population moves primarily into the $J = 2$ state and $|C^{J=2\,\Omega\,M}|^2 \approx 0.10$. For the middle intensity, $I = 4 \times 10^8$ W/cm^2 (Figure 4.19(b)), $|C^{J=2\,\Omega\,M}|^2$ increases to 0.16. The depletion of the $J = 1$ (initial) state and simultaneous population of higher-lying J

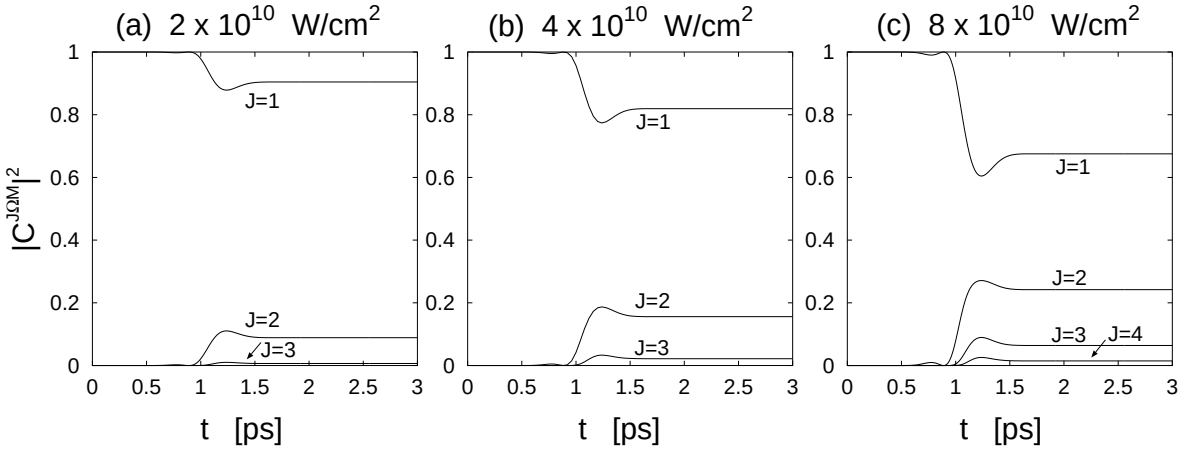

Figure 4.19: Depletion of the $J = 1$ rotational state, $|C^{J=1\,\Omega\,M}|^2$ and population of higher-lying J states, for three different intensities, $I = 2$, 4, and 8×10^8 W/cm^2, at $T = 0$ K. The pulse applied is the same as that described in Figure 4.17.

states is greatest for the most intense pulse, $I = 8 \times 10^8$ W/cm^2, shown in Figure 4.19(c).

$|C^{J=1\,\Omega\,M}|^2$ drops to almost 0.60, and then recovers to $\sim$0.67 after the peak of the applied laser field. $|C^{J=2\,\Omega\,M}|^2$ increases to 0.24 and the $J=3$ state also becomes populated, with $|C^{J=3\,\Omega\,M}|^2$ growing to 0.07.

The intensity, and thus the composition of the rotational wave packet directly affects the degree of molecular orientation, as shown in Figure 4.20. At $t=0$, $\langle\cos\theta\rangle_T(t)\approx 0$ for all three intensities. The highest intensity pulse ($I = 8 \times 10^8$ W/cm^2) gives rise to the largest degree of orientation, $|\langle\cos\theta\rangle_T(t)| \approx 0.34$, with reduced orientation observed for the less intense pulses. After the field is turned off (for $t > (t_0 + \sigma)$), the wave packet composition remains constant, although the relative phases of the rotational states continue to clock on the time scale of the rotational period. This dephasing and rephasing of the rotational states gives rise to rotational revivals that are observed over long ($t \gg \sigma$) times. The two-level beat pattern is present for all three pulse intensities, and the phases of the wave packets are not shifted, so revivals are also present in the sum of the curves shown in Figure 4.20.

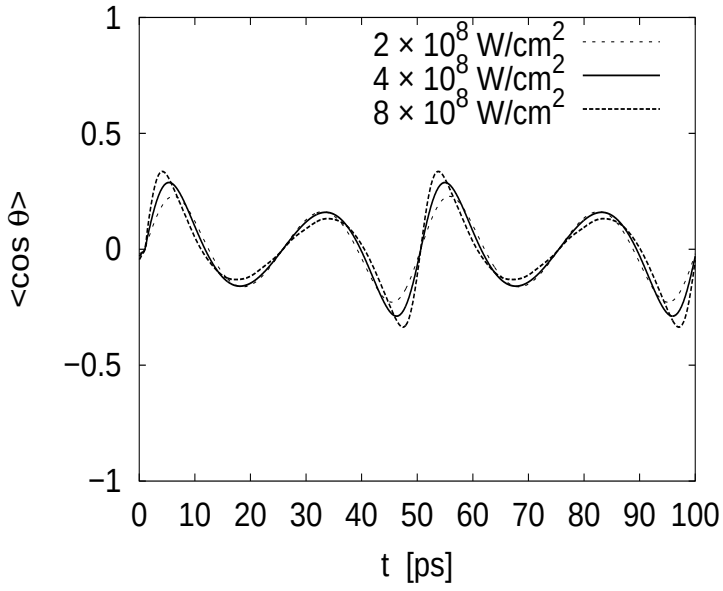

Figure 4.20: Orientation of OHF^- at $T = 0$ K, given by the orientation parameter $\langle\cos\theta\rangle_T(t)$, after application of a HCP with intensity $I = 2$, 4, and 8×10^8 W/cm^2. The pulse applied is the same as that described in Figure 4.17.

The effect of the field strength on molecular orientation can also be explained qualitatively in classical terms. The dipole moment feels the direction of the electric field and the consequence is angular motion in the direction of the field in the space-fixed frame. The angle θ between the dipole vector and the polarization direction becomes restricted to a narrow range, and molecular librations are limited. For higher intensities, the torque applied to the system is larger, so the resulting orientation is more pronounced.

Next, we will examine the effect temperature plays on molecular orientation.

Temperature dependence

We have seen in Figures 4.19 and 4.20 that increasing the field strength leads to a higher degree of molecular orientation. For these simulations, the temperature was kept at $T = 0$ K. In reality, however, the temperature of a molecular beam is greater than $T = 0$ K. Therefore, we will now examine how the wave packet behavior changes for various temperatures. For non-zero temperatures, rotational (J) levels are populated

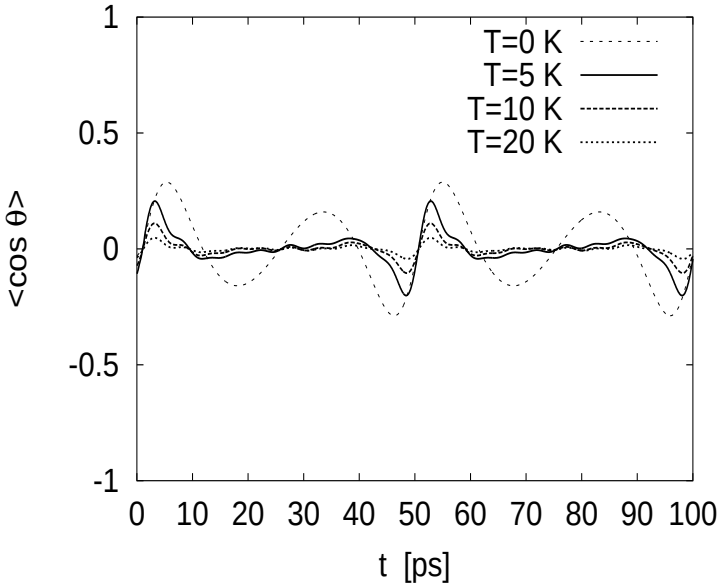

Figure 4.21: Orientation of OHF^- for $I = 4\times10^8$ W/cm^2, given by the orientation parameter $\langle\cos\,\theta\rangle_T(t)$, after application of a HCP with temperatures, $T = 0$, 5, 10, and 20 K. The pulse applied is the same as that described in Figure 4.17.

according to Boltzmann weights (described in Section 2.5.3), and an isotropic distribution of magnetic states is present for each initial state J_i, $-J_i \leq M_i \leq J_i$. The thermal average is therefore a weighted sum of time-dependent terms with different oscillation frequencies and phases (see Eq. (2.236). This thermal averaging implies that the orientation effects observed at lower temperatures will be partially diminished for higher temperatures. In Figure 4.21, the orientation cosine is shown for four temperatures, $T = 0$,5, 10, and 20 K. For $T = 0$ K, the orientation reaches the largest absolute value, ~ 0.3. One also sees from Figure 4.21 that the phases of the eigenstates corresponding to different temperatures are not shifted, so revivals are present in the sum of the four curves. As the temperature is increased, population is initially spread over several J states according to the Boltzmann distribution, such that a greater distribution in M_i states is present and the observed orientation decreases. An increase in field strength could counteract this

effect by imparting the system with enough angular momentum to overcome this thermal averaging.

In general, the fraction of molecules in the Jth rotational state is given by

$$\frac{n_J}{n} = \frac{(2J+1)e^{-BJ(J+1)/k_BT}}{Q_{\mathrm{rot}}(T)} \tag{4.18}$$

where n_J is the number of molecules in the Jth state and n is the total number of molecules [162]. The state with the highest weight, $J_{\max}$ (rounded to the closest integer), can be obtained by differentiating Eq. (4.18) with respect to J and setting equal to zero,

$$\frac{d\,(n_J/n)}{dJ} = 0. \tag{4.19}$$

Solving for $J_{\max}$, one arrives at

$$J_{\max} = \sqrt{k_BT/2\,B} - 1/2. \tag{4.20}$$

For $T = 5$, 10, and 20 K, $J_{\max}$ is found to be 2, 3, and 4, respectively.

We have shown that an IR HCP is able to orient a molecule by giving a "kick" of angular momentum along the field polarization direction. The resulting orientation of the molecular system is long (several picoseconds) compared to the time scale of vibrational motion (fs). Rotational revivals due to the dephasing and rephasing of the rotational eigenstates appear on the time scale of the rotational period, which is 49.6 ps for OHF^-. These revivals recur as long as coherence in the wave packet is maintained. For non-zero temperatures, or conditions typically found in molecular beams, the broader distribution of initial states J_i and thus M_i states slightly reduces the degree of orientation, but coherence in the rotational wave function is conserved. Having investigated the degree of orientation resulting from HCPs applied to our model system, we can proceed now to the challenge of selectively breaking the bonds of OHF^- using few-cycle pulses.

4.4.2 Breaking the strong and weak bonds

Previous studies have shown that the dissociation dynamics of OHF^-—in absence of pre-excitation—heavily favor the products O + HF [93], *i.e.* instantaneous excitation of the ground state vibrational wavefunction v_{00} of OHF^- to the neutral PES $V_n(\equiv V(OHF))$, and subsequent field-free propagation results in a branching ratio of 0.7 : 0.3 [93]. The same procedure carried out on our UMP4 PES results in a branching ratio of 0.84 : 0.16 at $t = 50$ fs for (O + HF):(OH + F), as shown in Figure 4.22. In other words, the O–H bond is weaker than the H–F bond. This difference in bond strength is

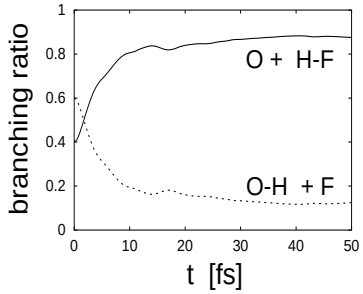

Figure 4.22: Instantaneous excitation of the ground state vibrational wave function υ_{00} of OHF^- to the neutral PES V_n results in the wave function $\Psi_n(t)$. Field-free propagation of $\Psi_n(t)$ on the PES of OHF results in a branching ratio of $0.84:0.16$ at $t = 50$ fs for O + HF products (solid) versus OH + F (dotted).

confirmed by measurements of the diatomics molecules; dissociation energies of OH and HF have been measured at 4.39 eV and 5.87 eV, respectively [97]. The question we ask, therefore, is whether this natural branching ratio can be changed using few-cycle laser pulses. Specifically, is it possible to enhance the branching ratio of (O + HF):(OH + F) to 100 : 0? More importantly: can we reverse the branching ratio and obtain a majority of products OH + F? We now proceed to investigate the answers to these questions.

The approach we take is analagous to the method we discussed with the previous system, FHF^-. We begin with the ground vibrational wave function of OHF^-, υ_{00}, for which the equilibrium geometry is calculated to be $R_1 = R_{OH} = 1.07$ Å, and $R_2 = R_{HF} = 1.38$ Å. Next, we design a few-cycle IR laser pulse that achieves maximum extension and compression of the bonds and thus a maximum displacement of the wave function from its equilibrium position. The laser field $E(t)$, as described in Eq. (4.8), has a $\sin^2$-shape. As in previous applications, the field strengths of both IR and UV pulses are chosen such that the intensity is below the Keldysh limit of $\sim 10^{13}$ W/cm^2, a limit above which double ionization or Stark shifts could occur [127]. The field strength of the IR pulse, $E_{0,\mathrm{IR}}$, is chosen to be 3.2 GV/m, and that of the UV pulse, $E_{0,\mathrm{UV}} = 5.0$ GV/m. The frequency of the IR pulse, $\omega_{\mathrm{IR}} = 1565$ cm^{-1} (relative frequency bandwidth $\Delta\omega_{\mathrm{IR}}/\omega_{\mathrm{IR}} = 0.03$), is tuned to drive the asymmetric stretching vibration, or the motion of the hydrogen between the O and F atoms. The phase, φ_{IR}, is set to 0, the pulse delay is $t_{0,\mathrm{IR}} = 0$ fs, and the pulse duration is $t_{p,\mathrm{IR}} = 50$ fs. Snapshots of the wave packet dynamics under the influence of these pulses are shown in the left panels of Figure 4.23, (a)-(e).

As in the limit of half-cycle pulses, each of the half optical cycles under the pulse envelope gives a strong kick to the H atom, exciting a superposition of several vibrational eigenstates. After a time delay of 19 fs, the wave packet created by the IR pulse has been displaced from the equilibrium position and R_{OH} has been extended from 1.10 Å

to 1.28 Å (see Figure 4.23(b)). This time corresponds with almost the end of the first complete cycle of the IR pulse and therefore to almost the maximum amplitude of the H atom oscillation. If an ultrashort UV pulse is now applied, it will photodetach an electron and prepare a wave packet on the surface of the neutral species, V_n, along the O + HF dissociation channel, see Figure 4.23(c). In fact, it is preferable to excite the anion system a few fs before the first IR cycle is completed, so that the maximum displacement of the H atom coincides with maximum pulse intensity. Accordingly, at $t_{0,\mathrm{UV}} = 19$ fs, a UV pulse is applied with duration $t_{p,\mathrm{UV}} = 5$ fs, a phase $\varphi_{\mathrm{UV}} = 0$, and a carrier frequency corresponding to the energy spacing between $V_a(\equiv V(OHF^-))$ and V_n, $\omega_{\mathrm{UV}} = 28\,228$ cm^{-1} $\equiv$ 3.5 eV (relative frequency bandwidth $\Delta\omega_{\mathrm{UV}}/\omega_{\mathrm{UV}} = 0.02$). Now, the wave packet evolves almost exclusively along the O + HF dissociation channel, as illustrated in the snapshots of Figure 4.23(c)-(e).

At the end of the propagation, at $t = 50$ fs, the wave packet remains relatively compact and the final calculated branching ratio of O + HF at $t = 50$ is 0.95 : 0.05 (see Figure 4.24(b)). For times $t > 50$ fs, the wave packet approaches the grid edge ($R_{\mathrm{OH}} = 4.0$ Å) and begins to be "eaten" by the gobbler function. Therefore, branching ratios are only reported for times $t < 50$ fs, before the norm of the wave function begins to change. For times $40 < t < 45$ fs, the branching ratio can be calculated and is found to be 0.95 : 0.05, an enhancement of $\sim$10% from the original 0.84 : 0.16. Thus, the products O + HF are heavily favored. As mentioned in Section 4.3.4, the absolute phase of the IR pulse, φ_{IR}, determines the direction in which the initial wave packet, $\Psi_a(t = 0)$, begins oscillating. In other words, for the same laser pulse shown in Figure 4.24(a) but with a phase $\varphi_{\mathrm{IR}} = \pi$, the first maximum extension of R_{OH} (compression of R_{HF}) occurs at $t = 31.5$ fs. Thus, the phase of the IR pulse inherently dictates the time at which the UV pulse is fired, $t_{0,\mathrm{UV}}$.

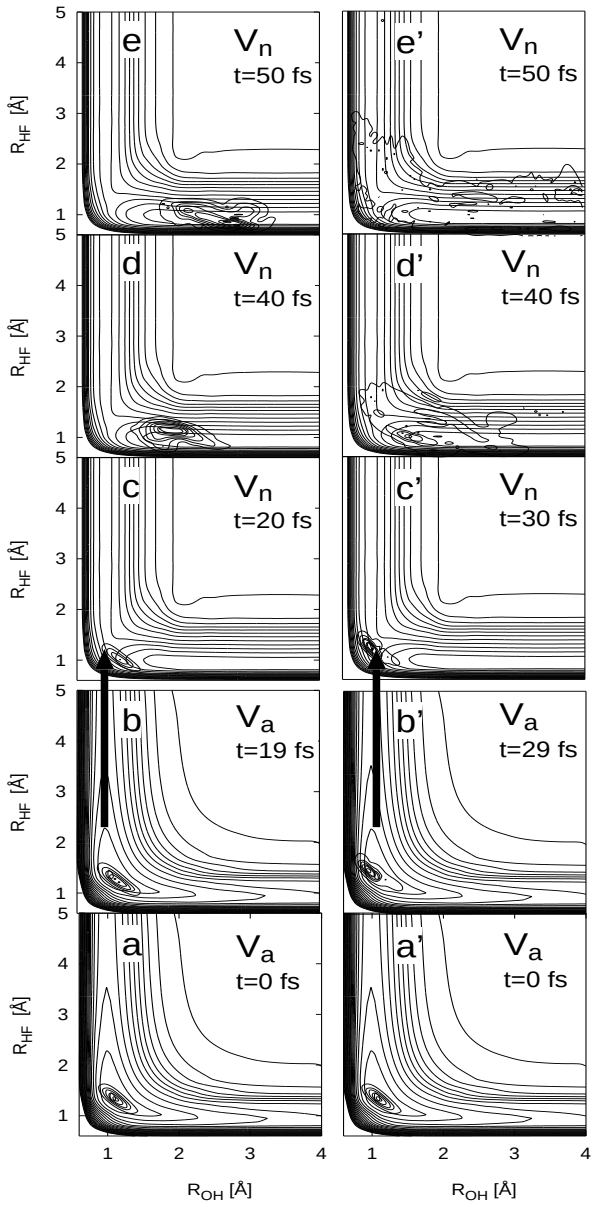

Figure 4.23: Attempt of selective breaking of the weak O–H bond (left panels, (a)-(e)) and strong H–F bond (right panels, (a')-(e')) of OHF, using few-cycle IR + UV laser pulses. In (a) and (a'), the vibrational ground state wave function superimposed on $V_a(\equiv V(OHF^-))$ is shown at $t = 0$ fs; (b) and (b') show the wave function during the few-cycle IR pulse, just before firing the UV pulse. Snapshots (c)-(e) and (c')-(e') show the time evolution of the wavefunction on V_n after the UV excitation.

Breaking the O–H bond

IR pulse parameters: $E_{0,\mathrm{IR}} = 3.2$ GV/m, $\omega_{\mathrm{IR}} = 1565$ cm^{-1}, $\varphi_{\mathrm{IR}} = 0$, $t_{0,\mathrm{IR}} = 0$ fs, and $t_{p,\mathrm{IR}} = 50$ fs.

UV pulse parameters: $E_{0,\mathrm{UV}} = 5.0$ GV/m, $\omega_{\mathrm{UV}} = 28\,228$ cm^{-1}, $\varphi_{\mathrm{UV}} = 0$, $t_{0,\mathrm{UV}} = 19$ fs, and $t_{p,\mathrm{UV}} = 5$ fs.

Breaking the H–F bond

IR pulse parameters: $E_{0,\mathrm{IR}} = 5.0$ GV/m, $\omega_{\mathrm{IR}} = 1565$ cm^{-1}, $\varphi_{\mathrm{IR}} = 0$, $t_{0,\mathrm{IR}} = 0$ fs, $t_{p,\mathrm{IR}} = 50$ fs.

UV pulse parameters: $E_{0,\mathrm{UV}} = 8.0$ GV/m, $\omega_{\mathrm{UV}} = 52\,423$ cm^{-1}, $\varphi_{\mathrm{UV}} = 0$, $t_{0,\mathrm{UV}} = 29$ fs and $t_{p,\mathrm{UV}} = 5$ fs.

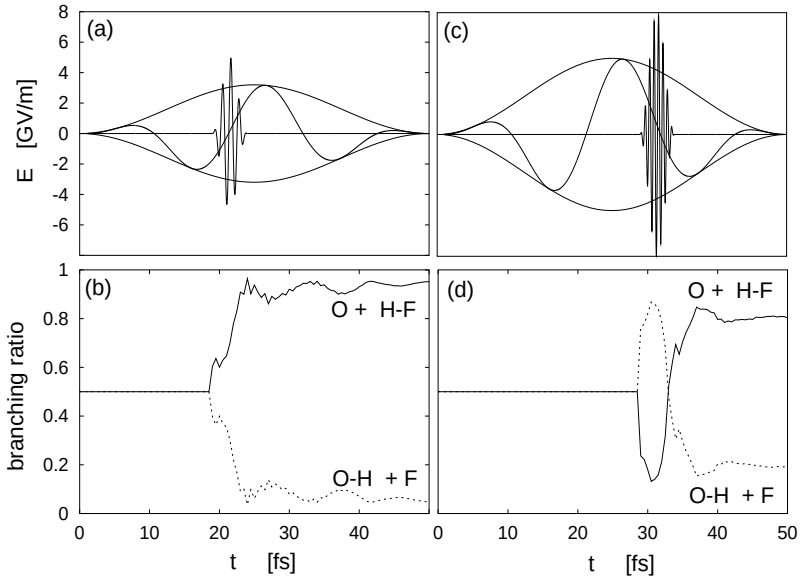

Figure 4.24:
Breaking the O–H bond:
(a) Few-cycle IR + UV laser pulses achieve maximum O + HF fragmentation.
IR pulse parameters: $E_{0,\mathrm{IR}} = 3.2$ GV/m, $\omega_{\mathrm{IR}} = 1565$ cm^{-1}, $\varphi_{\mathrm{IR}} = 0$, $t_{0,\mathrm{IR}} = 0$ fs, and $t_{p,\mathrm{IR}} = 50$ fs.
UV pulse parameters: $E_{0,\mathrm{UV}} = 5.0$ GV/m, $\omega_{\mathrm{UV}} = 28\,228$ cm^{-1}, $\varphi_{\mathrm{UV}} = 0$, $t_{0,\mathrm{UV}} = 19$ fs, and $t_{p,\mathrm{UV}} = 5$ fs.
(b) Time evolution of the branching ratio of the O + HF products (solid) versus OH + F (dotted).
Breaking the H–F bond:
(c) Few-cycle IR + UV laser pulses achieve maximum OH + F fragmentation.
IR pulse parameters: $E_{0,\mathrm{IR}} = 5.0$ GV/m, $\omega_{\mathrm{IR}} = 1565$ cm^{-1}, $\varphi_{\mathrm{IR}} = 0$, $t_{0,\mathrm{IR}} = 0$ fs, $t_{p,\mathrm{IR}} = 50$ fs.
UV pulse parameters: $E_{0,\mathrm{UV}} = 8.0$ GV/m, $\omega_{\mathrm{UV}} = 52\,423$ cm^{-1}, $\varphi_{\mathrm{UV}} = 0$, $t_{0,\mathrm{UV}} = 29$ fs, and $t_{p,\mathrm{UV}} = 5$ fs.
(d) Time evolution of the branching ratio of the O + HF products (solid) versus OH + F (dotted).

One can also examine the composition of the vibrational wave packet that is prepared by the IR pulse to see which eigenstates are present. In Figure 4.25, the populations of individual vibrational eigenstates are shown over the propagation time of 50 fs. The system begins in the ground vibrational state, v_{00}, and as the IR pulse is applied, population begins to migrate into other low-lying vibrational states, mostly into those with asymmetric stretching character. The population of v_{00} drops to 0.46 while v_{01} (asymmetric stretch) climbs to 0.30. Other significant contributions are from the first mixed-mode (symmetric + asymmetric stretches) v_{11} ($\sim$ 0.03) and the first excited asymmetric stretch, v_{02} ($\sim$0.08). The total population in the ground state of the anion (norm) decreases minimally to $\sim$0.98 shortly after the UV pulse (described in Figure 4.24(a)) is fired at $t = 19$ fs.

More challenging is to reverse the natural branching ratio and hence to enhance the fragmentation of the stronger bond, thereby producing OH + F species. The laser field is re-optimized for this purpose, and the resulting time evolution of the wave packet is shown in the right panels (a'-e') of Figure 4.23. Since the IR pulse in the previous case was optimized to drive the asymmetric stretching vibration and create

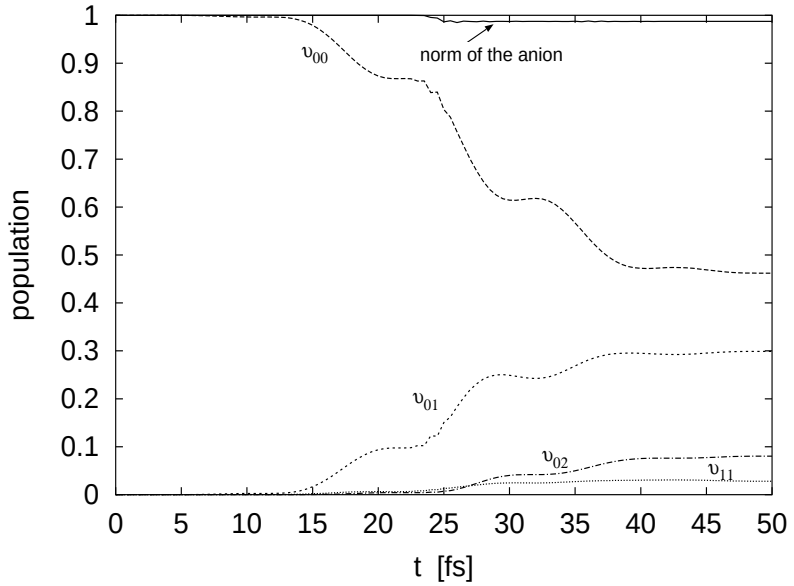

Figure 4.25: Generation of a vibrational wave packet from the few-cycle IR pulse shown in Figure 4.24(a). IR pulse parameters are: $E_{0,\mathrm{IR}} = 3.2$ GV/m, $\omega_{\mathrm{IR}} = 1565$ cm^{-1}, $\varphi_{\mathrm{IR}} = 0$, $t_{0,\mathrm{IR}} = 0$ fs, and $t_{p,\mathrm{IR}} = 50$ fs. Dominant contributions are from vibrational eigenstates υ_{00}, υ_{01} (asymmetric stretch), υ_{02} (first excited asymmetric stretch), and υ_{11} (symmetric + asymmetric). Depletion of population in the anion (OHF^-) ground state begins shortly after $t = 19$ fs, when the UV pulse is fired. The UV pulse parameters are $E_{0,\mathrm{UV}} = 5.0$ GV/m, $\omega_{\mathrm{UV}} = 28\,228$ cm^{-1}, $\varphi_{\mathrm{UV}} = 0$, $t_{0,\mathrm{UV}} = 19$ fs, and $t_{p,\mathrm{UV}} = 5$ fs. After vertical excitation of population to V_n, anion population (norm) drops to $\sim$0.98.

a dynamical wave packet that oscillates with the largest magnitude away from the equilibrium position, the frequency and pulse duration of the IR pulse are maintained. As expected, the composition of the resulting vibrational wave packet is nearly identical to the one generated in the previous case (shown in Figure 4.25). Due to the asymmetry of the potential, in order to maximize the OH + F products, the field strength has be to increased from $E_{0,\mathrm{IR}} = 3.2$ GV/m to $E_{0,\mathrm{IR}} = 5.0$ GV/m. More important, the timing and frequency of the UV laser pulse must be re-optimized such that the wave packet is excited at a different time, namely when the R_{HF} bond has been maximally extended, and with a different vertical energy, in this case one that is resonant with the OH + F dissociation channel of V_n. After 29 fs, the wave packet has almost reached the opposite turning point of its oscillation, such that R_{HF} is extended from 1.30 Å to 1.41 Å (Figure 4.23(b')). At $t_{0,\mathrm{UV}} = 29$ fs, the UV pulse is applied (Figure 4.24(c)) with an optimized carrier frequency, $\omega_{\mathrm{UV}} = 52\,423$ cm^{-1} $\equiv$ 6.5 eV (relative frequency bandwidth $\Delta\omega_{\mathrm{UV}}/\omega_{\mathrm{UV}} = 0.01$), roughly twice the frequency required in the previous case. The pulse duration $t_{p,\mathrm{UV}} = 5$ fs remains the same, and the electric field strength is increased, from $E_{0,\mathrm{UV}} = 5.0$ GV/m to $E_{0,\mathrm{UV}} = 8.0$ GV/m. The wave packet evolution along the V_n surface is shown in Figure 4.23(c'-e').

The vertical excitation of the compact displaced wave packet at $t = 29$ fs from V_a to V_n is followed by its spreading in both dissociation directions. The wave packet is not confined to the OH + F dissociation channel due to the shallow slope of the PES in this region. At $t = 40$ fs, the wave packet begins traveling outward toward the center of V_n, while also rapidly descending the dissociation path O + HF. By $t = 50$ fs (Figure 4.23(e')), the wave packet has reached the grid edge, $R_{OH} = 4.0$ Å, so branching ratios calculated at $t \geq 50$ fs are unreliable. At $t = 40$ fs (Figure 4.23(d')), the branching ratio (O + HF):(OH + F) is calculated to be 0.80 : 0.20. This result demonstrates a marginal (4%) enhancement of the product OH + F from 0.84:0.16, which was found for the pure vertical excitation of OHF^- without the few-cycle IR pre-excitation. Therefore, the goal of selective bond breaking of OHF^- in favor of the products OH + F could not be achieved using this approach of combined IR + UV laser pulses. Alternate methods for improving the selectivity of dissociation products will be discussed in Chapter 5.

4.5 Assumptions and sources of error

In the quantum dynamical calculations discussed in the previous sections, certain assumptions were invoked to simplify the model systems that were studied. In this section, these assumptions and possible resulting errors will be discussed.

Bending vibration and rotations

One of the most basic assumptions made throughout all simulations is that the anion and neutral molecules are linear species; the bending angle γ, shown schematically in Figure 4.26, was set to 180° such that $\cos(\gamma)$ in the kinetic portion of the Hamiltonian from Eq. (3.3) is -1. In other words, bending vibrations were neglected throughout

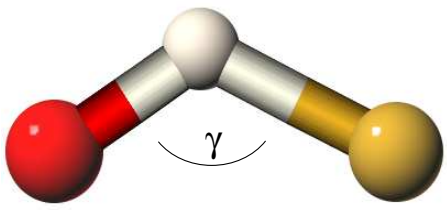

Figure 4.26: Schematic representation of the bending vibration of a triatomic molecule.

the calculations. This assumption is valid as long as the frequency of the bending

vibration is considerably different from that of the stretching vibrations—symmetric and asymmetric—which were accounted for in the 2D model systems. If this condition is not met, then a finite probability exists that the laser pulse energy will drive vibrational motion with similar frequencies to those which were accounted for in the model. In our laser-driven control simulations, absorption of laser energy by other vibrational modes could greatly reduce the efficacy of the dynamical symmetry breaking that results from the IR laser pulse. To estimate the probability that laser energy will excite vibrational modes with commensurate frequencies, *i.e.* bending vibrations, let us compare the harmonic vibrational frequencies for FHF^- and OHF^-; these frequencies were listed in Table 3.3 and Table 3.9, respectively.

For FHF^-, the four vibrational frequencies are $\nu_1 = 649$ (sym), the doubly degenerate $\nu_2 = 1380$ (bend), and $\nu_3 = 1251$ (asym) cm^{-1} (*cf.* Table 3.3). The doubly degenerate bending vibrational frequency, which is the vibration of the center hydrogen axially away from its collinear position, is approximately 100 cm^{-1} higher than the asymmetric stretching vibration. The spread in energy of a 50 fs IR laser pulse, governed by the uncertainty principle (see Eq. (2.141)), is approximately $\Delta\omega_{IR} = 53$ cm^{-1}; for shorter pulses, this spread is even larger. Therefore, an IR laser pulse with a central carrier frequency tuned to drive the asymmetric stretching vibration may also drive other vibrational modes. An extension of the 2D model of FHF^- to include the bending vibration would therefore provide a more complete description of the vibrational dynamics and resulting bond-selective dissociation. In the case of OHF^-, the four harmonic vibrational frequencies of OHF^- are $\nu_1 = 477$ (sym), $\nu_2' = 1059$ and $\nu_2'' = 1238$ (bend), and $\nu_3 = 1698$ (asym) cm^{-1} (*cf.* Table 3.9). The frequencies of the bending vibrations are more than 400 cm^{-1} lower than the asymmetric stretching and would be unaffected by a 50 fs IR pulse tuned to an energy $\omega_{IR} = 1565$ cm^{-1}. Nonetheless, extending the model to include the bending angle γ would contribute additional anharmonicity to the calculated frequencies.

The possibility of exciting bending vibrational modes should be distinguished from *internal vibrational energy redistribution* (IVR) that can occur between the nuclear degrees of freedom. In the former case, the laser would simultaneously excite both the stretching and bending vibrations due to the fact that their fundamental frequencies are similar. IVR, on the other hand, refers to the gradual dissipation of energy from a specific vibrational mode to other modes. This phenomenon typically occurs over a time scale of $10^{-12} - 10^{-13}$ s [133]. Since our simulations take place on the order of $10^{-13} - 10^{-14}$ s, IVR should not be a significant source of energy dissipation.

The neglect of rotations in the quantum dynamical simulations of FHF^- and OHF^-

should be a good approximation since the rotational periods of both molecules are much longer than the vibrational periods, $\tau_{\text{rot}} \gg \tau_{\text{vib}}$. For FHF^-, the rotational period can be calculated from the rotational constant $B = 0.341$ cm^{-1} (see Table 2.204), and is found to be $\tau_{\text{rot}} = \pi\hbar/B = 51.3$ ps; OHF^- has a rotational period of 49.6 ps. The dynamical symmetry breaking and subsequent bond-selective dissociation processes take place on a time scale of $\sim$100 fs.

Transitions from V_n to V_a

As discussed in Section 4.2, the laser intensity is kept low enough ($< 10^{13}$ W/cm^2) such that a maximum of $\sim 10\%$ of the population is excited from the anionic PES V_a to the neutral PES V_n. This low laser intensity ensures that the artificial back-transfer of population from V_n to V_a is kept to only $\sim 1\%$. Since the initial UV-excitation of population to V_n corresponds to the photodetachment of an electron, this back-transfer would imply the re-attachment of an electron to the molecule, a process that is unrealistic under normal experimental conditions. Therefore, in the simulations presented here, any flux of population from the neutral PES to the anionic PES is an artifact of the model. However, due to the moderate laser intensities used here, this back-transfer can be considered negligibly small.

Vibrational transitions within V_n

In the bond-selective dissociation simulations discussed here, the permanent dipole moment of the neutral system, μ_n, was set to 0 for both FHF and OHF, so vibrational transitions within the neutral PES, V_n, were not considered. In other words, the wave function that evolves on V_n, $\Psi_n(t)$, is assumed to be invariant to any IR laser frequencies. In reality, any laser frequencies resonant with gaps between vibrational levels in V_n would be able to induce transitions between these states. This phenomenon has already been studied in depth experimentally [80, 81, 82, 83, 84]. Thus, in the future, one should extend the model of the neutral system to include the permanent dipole moment of the neutral species, μ_n, and thus account for vibrational transitions within V_n. This extension would also allow for the design of new laser control schemes that rely on transitions between vibrational eigenstates in the neutral system. These transitions could, in fact, be used to enhance product yields in a specific dissociation channel. For example, in the case of OHF, excitation of a vibrational eigenstate that is localized along the H–F bond could be used to drive population along the dissociation channel OH +F and increase the branching ratio in favor of those products.

Controlling the absolute carrier envelope phase

Controlling the absolute carrier envelope phase of the IR pulse is critical for the control of few-cycle laser-driven wave packets because the system is sensitive to the electric field rather than to the pulse intensity [163]. In our simulations, the timing of the second pulse, the UV photodetachment pulse, is tuned based on the position of the wave packet during or shortly after the IR pulse. To understand this dependence of the UV pulse on the IR pulse, let us examine the properties of the IR field in more detail. For an IR frequency that is tuned to drive a particular vibrational motion, the field strength determines the amplitude of the displacement of wave packet. Similarly, when the laser is turned on, the sign of the field determines the direction in which the wave packet begins oscillating. In other words, the profile of the electric field within the pulse envelope is critical in steering the motion of the wave packet. The field profile contained in the pulse envelope is determined by the pulse carrier phase. To demonstrate the significance of the carrier phase, laser pulses with the same field strength, frequency, and shape function, but with *different carrier phases*, $\varphi = 0$, $\varphi = \pi/2$, and $\varphi = \pi$, are shown exemplarily in Figure 4.27 for an electric field given by,

$$\vec{E}(t) = \begin{cases} \vec{\varepsilon} E_0 \cos(\omega t + \varphi) \sin^2\left(\frac{\pi(t-t_0)}{t_p}\right) & t_0 \leq t \leq (t_0 + t_p) \\ 0 & \text{otherwise.} \end{cases} \tag{4.21}$$

For all three pulses, $\omega = 31\,3024$ cm^{-1}, $t_0 = 0$ fs, and $t_p = 20$ fs. One sees immediately

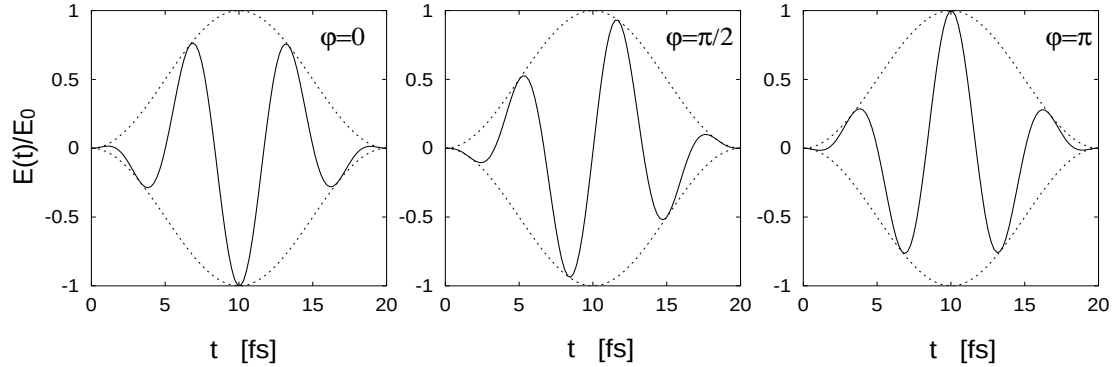

Figure 4.27: The electric field profile of the laser pulses consisting of very few optical cycles depends on the phase φ of the carrier frequency with respect to the pulse's envelope; the maximum of the electric field points in opposite directions at $t = 10$ fs for $\varphi = 0$ and $\varphi = \pi$.

that the field profiles are quite different. For $\varphi = 0$, for example, the electric field has negative amplitudes at the beginning of the pulse, $E(t) < 0$, and it contains a maximum amplitude at $t = 10$ fs with a negative field strength. In the case for which $\varphi = \pi$, the pulse begins with $E(t) > 0$, and its maximum amplitude is reached at $t = 10$ fs with positive field strength. For $\varphi = \pi/2$, the pulse profile is asymmetric and contains two peaks of almost equal height but of opposite field strength. In other words, depending on the phase of the

IR field, a molecule would experience very different electric field profiles. As a result, the wave packet being driven by the pulse for which $\varphi = 0$ will be located at very different region of the PES than would a system driven by a pulse with $\varphi = \pi$. The UV laser is designed to fire when the position (or momentum, see Ref. [33]) of the wave packet is optimal to result in bond-selective dissociation. This condition implies that the system experiences the maximum field strength contained in the pulse envelope. Depending on the IR carrier phase, however, this maximum will occur at varying times. Therefore, the phase of the IR field must be controlled in order to achieve reproducible results. Otherwise, when the subsequent UV laser is fired, the tuned pulse may fail to excite a significant population to the desired dissociation channel. In the application that has been discussed in this work, for which the few-cycle IR pulse is designed to create dynamical symmetry breaking, this phase control—in addition to precise timing—is critical for bond-selective dissociation. The experimental implementation of these suggested few-cycle pulses requires the reproducible generation of pulses with the same absolute phase. Recent progress in the development of few-cycle pulses has indicated that stabilizing and even controlling the carrier envelope phase of attosecond x-ray [130, 164] and femtosecond, near-IR ($800-1700$ nm) lasers is possible [129, 165, 166].

Alignment and orientation effects

Unless explicitly stated otherwise, the orientation of the triatomic systems used throughout all simulations was assumed to be known. In other words, the molecules were assumed not only to be aligned parallel to the electric field polarization vector (Z), but they were also taken to be oriented in either the $+Z$ or $-Z$ direction. Within this approximation, laser-induced dissociation dynamics are simulated, and predictions are made regarding the spatial separation of products within the laboratory (space-fixed) frame. In laboratory experiments involving an ensemble of molecules in the gas phase, the species are randomly oriented. The tuned IR laser pulses would be ineffective at exciting molecules of non-parallel alignment (see Figure 4.14). As a result, the UV laser pulses would only be successful at exciting a small fraction of the total sample. Nonetheless, this small fraction would undergo electron photodetachment and the subsequent dissociation products would be spatially separated, as achieved for species of fixed orientation (see Figure 4.15).

The effectiveness of the proposed combined few-cycle IR + UV laser pulses therefore depends greatly on the orientation of the reactant species. To characterize this problem, we first examined orientation-dependent dissociation dynamics in Section 4.3.7. Later, in Section 4.4.1, we designed half-cycle IR pulses to control the orientation

of OHF^- over a long (picoseconds) time period—much longer than the time scale of femtosecond laser pulse control schemes. Nonetheless, in these simulations, we neglected the spin $\frac{1}{2}$ of the anion that gives rise to a doublet multiplicity, $^2\Pi$, and just considered the electronic orbital angular momentum, $L = 1$, corresponding to the state $^1\Pi$. The simulations should be repeated to see the effect of spin angular momentum on the rotational wave packet dynamics. In addition, the rotational energy levels of a $^2\Pi$ rigid rotor, containing electronic orbital momentum and spin angular momentum, differ from those of a $^1\Sigma$ rigid rotor. The $^2\Pi$ energy levels contain a spin-orbit interaction term, $\mathcal{A}$, and one can show that the levels are given as [142, 167],

$$E(^2\Pi) = B\left[\left(J - \frac{1}{2}\right)\left(J + \frac{3}{2}\right) \pm \frac{1}{2}\mathcal{X}\right] \tag{4.22}$$

where

$$\mathcal{X} = \left[4\left(J + \frac{1}{2}\right)^2 + \frac{\mathcal{A}}{B}\left(\frac{\mathcal{A}}{B} - 4\right)\right]^{\frac{1}{2}}. \tag{4.23}$$

For increasing rotation, the contribution from the spin-orbit coupling term decreases, so for large J values, one can assume the $^1\Sigma$ rigid rotor energy levels are valid. However, for decreasing rotation, the spin-orbit coupling should be accounted for. In the future, therefore, the calculations discussed in this thesis should be repeated using the $^2\Pi$ rigid rotor energy levels.

One controversial aspect of controlling molecular orientation using half-cycle pulses is the role of the polarizability, or induced dipole. As discussed in Section 2.5.3, neglecting the polarizability should be valid for the special case of a HCP of moderate intensity ($< 10^{13}$ W/cm^2) used in this thesis [145]. Nonetheless, according to B. Friedrich, for high intensities, the induced dipole interaction could become important [168]. Due to the $\cos^2$ nature of the induced dipole interaction potential, however, the *alignment* rather than the orientation of the system is enhanced. Since alignment does not distinguish between "head" and "tail" of the molecule, an aligned molecule experiences angular confinement about the space-fixed Z axis, with equal probability of being aligned in the $+Z$ and $-Z$ directions. Thus, for increased field strengths, the alignment may become enhanced while the orientation may be diminished. For such high-intensity pulses, one could thus study the effect of the combined dipole/polarizability interaction on the wave packet dynamics .

Temperature

Temperature was only explicitly discussed in this work in the context of characterizing molecular orientation, $\langle \cos\theta \rangle_T$, for a Boltzmann spread of energies (see Section 4.4.1).

That is, all other quantum dynamical simulations assumed a temperature $T = 0$ K, or a "rotationally cold" sample of molecules. Thermal energies, $k_B T$, are on the order of 190 cm^{-1} for room temperature. These energies are well below the vibrational energies ($\sim$1500 cm^{-1}) that were considered in the simulated molecular dynamics, so they should not affect the results. Rotational energies, on the other hand, are indeed much smaller than vibrational energies and typically in the domain of thermal energies. Accordingly, the temperature dependence of molecular orientation was examined for small ($T < 50$ K) temperatures in Section 4.4.1.